Soft Matter

Penetrant shape effects on activated dynamics and selectivity in polymer melts and networks based on self-consistent cooperative hopping theory

Journal:	*Soft Matter*
Manuscript ID	SM-ART-08-2023-001139.R1
Article Type:	Paper
Date Submitted by the Author:	16-Oct-2023
Complete List of Authors:	Mei, Baicheng; University of Illinois at Urbana-Champaign, Schweizer, Kenneth; University of Illinois at Urbana-Champaign,

Penetrant shape effects on activated dynamics and selectivity in polymer melts and networks based on self-consistent cooperative hopping theory

Baicheng Mei [a,d] and Kenneth S. Schweizer [*a,b ,c,d]

[a.] *Department of Materials Science, University of Illinois, Urbana, IL 61801, USA*

[b.] *Department of Chemistry, University of Illinois, Urbana, IL 61801, USA*

[c.] *Department of Chemical and Biomolecular Engineering, University of Illinois, Urbana, IL 61801, USA*

[d.] *Materials Research Laboratory, University of Illinois, Urbana, IL 61801, USA*

[*] kschweiz@illinois.edu

Abstract

We generalize and apply the microscopic self-consistent cooperative hopping theory for activated penetrant dynamics in polymer melts and crosslinked networks to address the role of highly variable non-spherical molecular shape. The focus is on vastly different shaped penetrants that have identical space filling volume in order to isolate how non-spherical shape explicitly modifies dynamics over a wide range of temperature down to the kinetic glass transition temperature. The theory relates intramolecular and intermolecular structure and kinetic constraints, and reveals how different solvation packing of polymer monomers around variable shaped penetrants impact penetrant hopping. A highly shape-dependent penetrant activated relaxation, including alpha time decoupling and trajectory level cooperativity of the hopping process, is predicted in the deeply supercooled regime for relatively larger penetrants which is sensitive to whether the polymer matrix is a melt or heavily crosslinked network. In contrast, for smaller size penetrants or at high/medium temperatures the effect of isochoric penetrant shape is relatively weak. We propose an aspect ratio variable that organizes how penetrant shape influences the activated relaxation times, leading to a (near) collapse or master curve. The relative absolute values of the penetrant relaxation time (inverse hopping rate) in polymer melts versus in crosslinked networks are found to be opposite when compared at a common absolute temperature versus when they are compared at a fixed value of distance from the glass transition based on the variable T_g/T with T_g the glass transition temperature. Quantitative comparison with recent diffusion experiments on chemically complex molecular penetrants of variable shape but fixed volume in crosslinked networks reveals good agreement, and testable new predictions are made. Extension of the theoretical approach to more complex systems of high experimental interest are discussed, including applications to realizing selective transport in membrane separation.

I. Introduction

Understanding and controlling the permeation of atoms, molecules, and even nanoparticles (referred to as "penetrants"), in dense and cold polymer melts, crosslinked networks, gels, and glasses is a rich scientific problem [1-24]. It underpins many materials science applications, such as gas and organic molecule separations [5-10], barrier materials for coatings [11, 12], self-healing based on polymeric microcapsules [11, 12], ion and solvent transport in biological and macromolecular materials [8, 13] and drug delivery [14-16]. Generally, the permeation coefficient is a combined effect of penetrant solubility and diffusion rate [17-19], but the latter is generally much more sensitive to chemistry and thermodynamic state since it is typically a strongly activated process. However, even in the *dilute* penetrant limit studied here, existing theoretical models are mostly phenomenological and built on the difficult to quantify concept of "free volume".[5, 8, 13, 20-24]

Our recent work has aimed to create a microscopic force based predictive statistical mechanical theory for penetrant activated dynamics, focused to date on spherical penetrants in hard sphere matrices [25, 26], polymer melts [27], and crosslinked polymer networks [28, 29]. Quantitative comparisons with experiment and simulations have revealed rather good agreements [25, 26, 29-32]. However, the explicit role of penetrant shape, which can be highly variable in real systems, has not been addressed, and is of high fundamental and experimental interest. In this article we extend and apply the theory to treat non-spherical molecular penetrants over a wide range of shapes in both polymer melts and networks, and from weakly supercooled states to the kinetic vitrification temperature. The focus is on the explicit dynamical consequences of shape, and hence different penetrants are analyzed at *fixed* molecular volume. This is a subtle, but important, problem given that our prior recent theoretical work [25], experimental studies [26, 29, 31], and simulations of others [19, 30] suggest penetrant volume is the crucial leading order variable determining the rate of activated hopping in polymeric media corresponding to a surprising degree

of "self-averaging" of molecular shape on the long Fickian diffusion time scales, at least for the limited class of penetrants studied.

The foundational starting point is to understand polymer matrix activated structural relaxation, which has been achieved based on the Elastically Collective Nonlinear Langevin Equation (ECNLE) theory [33, 34]. This theory causally relates interactions, thermodynamic state, and packing structure as embedded in a *dynamic* free energy that quantifies kinetic constraints to predict activated relaxation in colloids [33, 34], molecular and polymeric liquids [32, 35-39], and crosslinked networks [40]. The polymer alpha relaxation process is a coupled local-nonlocal activated process at the Kuhn statistical segment level, involving a local cage barrier (F_B) that quantifies the kinetic constraints from the surrounding segments and a nonlocal collective elastic barrier (F_{el}) that arises from correlated or facilitating small collective long-range displacements of all segments outside the cage that effectively dress the large amplitude hopping event [35, 36].

ECNLE theory has been extended to treat the activated dynamics of dilute hard sphere penetrants in a hard sphere matrix fluid, resulting in the Self-Consistent Cooperative Hopping (SCCH) theory [25, 26]. Recently it has been extended to semi-flexible polymer melts [27] and crosslinked network matrices [28, 29] for spherical penetrants. The penetrant barrier and mean hopping time, and the extent of coupling of its transport with the early, medium, and deeply supercooled stages of the matrix structural relaxation process, are predicted based on two *coupled* dynamic free energies [25-28]. The influence of various chemical and physical effects on the temperature/packing-fraction dependence of penetrant dynamics have been studied, including chain connectivity in polymers [27], degree of crosslinking in networks [28, 29]), attractive penetrant-matrix interactions [27], external stress [41] and penetrant size [26, 27, 29, 31]. Many of the theoretical predictions of SCCH theory agree well with simulations [19, 25, 29, 30] and experiments [29, 31].

Our present work is strongly motivated by a recent combined experiment-simulation-theory study [29] of the dependence of the alpha relaxation time and diffusion constant of dilute penetrants in crosslinked poly(n-butylacrylate) (PnBA) networks as a function of degree of crosslinking. It was found that the crosslinking fraction dependence of the penetrant diffusion constant (inverse alpha time) of the dye N,N'-Bis(2,5-di-tert-butylphenyl)-3,4,9,10-perylenedicarboximide (BTBP) exhibits an almost identical temperature dependence of that of the significantly different shaped tert-butylated rubrene (TBRb) penetrant. This rather surprising finding was interpreted as due to BTBP having a nearly identical space filling volume as that of TBRb, suggesting a remarkable degree of dynamical self-averaging of penetrant shape. However, it was also observed that the absolute value of TBRb diffusion constant is larger by a factor of ~3-5 at any fixed crosslink density and temperature than that of BTBP, which was attributed to the explicit penetrant shape effect. Understanding this finding is obviously beyond the scope of models that adopt a spherical particle description of penetrants. Considering the shape effect on penetrant activated relaxation in polymeric media is a broad, open, and challenging scientific problem that is highly germane to difficult membrane separation applications.

Here, we extend and apply to experiment the SCCH theory to address how penetrant shape influences its activated hopping over a very wide range of temperatures from the matrix glass transition temperature T_g through the wide deeply supercooled regime, and into the high temperature rubbery regime of polymer melts and crosslinked networks. Beyond an in-depth theoretical exploration of the role of penetrant shape in glass forming polymer melts and networks, another goal of the present article is to make predictions that can be tested (or a minimum motivate) in new experiments and simulations. The latter is discussed in some depth in section VIA, and a preview is as follows. (i) Our first focus is on how molecular shape *at fixed molecular volume*

affects the penetrant relaxation time and diffusion constant over a wide range of temperatures, and how crosslinking changes the thermal behavior compared to polymer melts. This exploration of temperature dependence is presented in the two common manners analyzed experimentally: as a function of absolute temperature, and in a "normalized" Angell-like representation as a function of inverse temperature rendered dimensionless by the polymer matrix glass transition temperature. (ii) Prior theoretical studies based on representing molecules as effective spheres have shown penetrant size relative to a key length of dynamical importance in the polymer matrix plays a crucial role in activated penetrant relaxation and diffusion. Most recently, two regimes of "small" and "large" penetrants have emerged based on our theoretical approach associated with to what extent penetrant hopping is coupled to the longer-range collective elasticity of the polymer matrix.[25, 29, 31] This advance frames our study in this article of the effect of molecular shape based on a careful choice of two values of penetrant volume that fall into the small and large categories. (iii) We search for a scalar metric that can organize the effect of molecular shape and propose a "penetrant aspect ratio" variable that provides significant insight. (iv) The mechanistic manner that penetrant shape determines the extent of coupling between the penetrant activated hopping event and a correlated dynamic reorganization of the polymer matrix is explored at both a mean trajectory level, and in terms of the experimentally observable "decoupling" ratio defined as the ratio of penetrant hopping time to the polymer alpha relaxation time. (v) The penetrant shape effects on the predicted exponential variation of relaxation time or diffusion constant as a function of the crosslink density dependent glass transition temperature is also studied.

Our theoretical studies of melts and crosslinked polymer networks are carried out to explore the relative importance on penetrant diffusivity of shape versus molecular volume over a range of temperatures and crosslink densities. This analysis is relevant to the subtle problem of

creating polymeric media (or membranes) that can separate molecules of essentially identical volume but different shapes based on differences of their activated hopping dynamics. Experimental and most simulation studies of the penetrant dynamics problem is often focused on mass transport, i.e., long time diffusion constant of penetrants.[2, 4, 19, 29, 30] We note that for an activated transport problem, what we call the penetrant relaxation time is basically the inverse of the mean hopping time that plays the critical role in determining the activated diffusion constant. This point has been recently discussed in detail within our theoretical approach [28], and successfully tested against experiments and simulations [29, 30]. This includes most recently a quantitative comparison of the penetrant relaxation time deduced from the incoherent dynamic structure factor (self-intermediate scattering function) on a local scale with the long-time diffusion constant [30]. These studies also establish the extent to which a crosslinked mesh in networks can modify penetrant diffusivity [28-30]. In this article we focus mainly on the penetrant relaxation time (inverse hopping rate) but for the aforementioned reasons the results are directly relevant to penetrant mass transport.

Sections II and III briefly describe the molecular models and statistical mechanical theories adopted, and extends them to treat shaped molecular penetrant packing structure and activated dynamics. Readers not interested in these technical details can skip these two sections and go directly to the results sections IV-VI which also discuss connections to experiments and simulations. Shape effects at several *fixed* penetrant space filling volumes on the temperature dependence of the penetrant alpha relaxation time is presented and analyzed in section IV for polymer melts and networks. The dynamical effects of shape are proposed to be largely captured by an aspect ratio variable that quantifies shape anisotropy. How penetrant shape impacts the degree of decoupling of the polymer and penetrant alpha times and the degree of trajectory-level

cooperativity associated with the hopping process is analyzed in Section V. Section VI summarizes our most important predictions that are testable in future experiments and simulations. A quantitative application of the theory to the recent experimental study mentioned above [29] is also presented. The article concludes with a summary and future outlook in Section VII. Supplementary Information (SI) presents some relevant and well-known theoretical background, and also additional calculations and figures that further support the results and the scientific conclusions that we draw in the main article.

II. Structural Correlations

In this and the next section we provide a brief description of the relevant theoretical methods employed for the new work in sections IV-VI. We emphasize that most of the technical details, equations, derivations, numerical implementations, and discussion of limitations of the theory tools employed have been thoroughly documented previously, especially in Refs. [27, 35, 40, 42, 43] for PRISM integral equation theory, [33-40] for ECNLE theory and [25-28] for SCCH theory; their detailed review is not repeated here and/or are briefly discussed in the SI. The primary technical novelty of the present paper is that it is the first to explicitly include penetrant shape effects in SCCH theory. In this section II we describe the molecular models and theory of structural correlations that enter the dynamic theories as input (discussed in section III).

A. Molecular models and structural correlations

Interaction site models are employed to model polymer chains and molecular penetrants. Intermolecular site-site structural pair correlation functions are computed using the Polymer Reference Interaction Site Model (PRISM) integral equation theory [42-45]. Polymers are modeled as discrete Koyama semiflexible chains (SFC) composed of tangent spherical beads (diameter σ, bond length $l_{\mathrm{b}} = \sigma$) [27, 44, 45] to compute the intramolecular structure factor $\omega_{\mathrm{m}}(q)$ required as input

to PRISM theory. The chain bending energy is chosen to yield a ratio of the persistence length to bead diameter (a local chain backbone "aspect ratio") typical of real flexible polymers, $\xi_p/\sigma = 4/3$.[27, 28, 35, 40, 44] Polymer sites interact via pure hard-core repulsions, and are studied under melt-like packing fraction conditions, $\phi_{eff} \equiv \rho\pi\sigma^3/6(1\text{-}\Delta_N)$ = 0.56-0.67 , where Δ_N is the site overlap correction in conformationally ideal Koyama model [44, 45]. The Percus-Yevick (PY) closure of the PRISM equations is adopted following prior work for the PnBA systems of present interest [28, 29]. The well tested mapping approach [36-38] for PnBA systems to convert packing fraction to temperature at 1 atm pressure is adopted (see SI). We note that within PRISM theory the elementary polymer unit is an interaction site (referred to as a monomer, subscript "m"), in contrast to the level of dynamical description which is at the Kuhn segment (indicated by subscript "K") level as discussed below and elsewhere [27, 28, 30, 36, 40, 46]. The relationship between intermolecular pair correlation functions of a Kuhn segment and a site or monomer is presented in the SI. As done previously [27, 35, 40], we set the number of sites in a Kuhn bead N_K equal to the ratio of Kuhn length l_K to bead diameter σ corresponding to $N_K = l_K/\sigma = 2\xi_p/\sigma = 8/3$.

Rigid molecular penetrants of fixed geometry are described at the interaction site level where all interactions sites are tangent and taken to be identical with the same hard-core diameter (d_s), i.e., the bond length equals the hard sphere site diameter. All interaction sites are treated as symmetry equivalent in applications of PRISM theory to predict intermolecular site-site pair correlations. The site-site molecule-polymer pair interaction is a pure hard-core repulsion. The penetrant intramolecular structure factor enters PRISM theory as input and is given by $\omega_p(q) = N_p^{-1}\sum_{\alpha,\theta=1}^{N_p}\sin(qr_{\alpha\theta})/qr_{\alpha\theta}$, where $r_{\alpha\theta}$ is the known scalar distance between sites α and θ within a rigid penetrant molecule that contains a total of N_p sites. We define an equivalent hard sphere model for each shaped penetrant where $\omega_p(q)$ equals unity with an effective diameter chosen to

reproduce the site-level space filling volume of the shaped penetrants corresponding to $d_{\text{eff}} \equiv N_{\text{p}}^{1/3}$ d_{s} for the tangent model. The values of d_{s} in units of the polymer monomer diameter for the different penetrant shapes studied is given in Table 1. Note the total volume of every shaped penetrant is *set to be identical* in order to focus explicitly on the role of molecular shape.

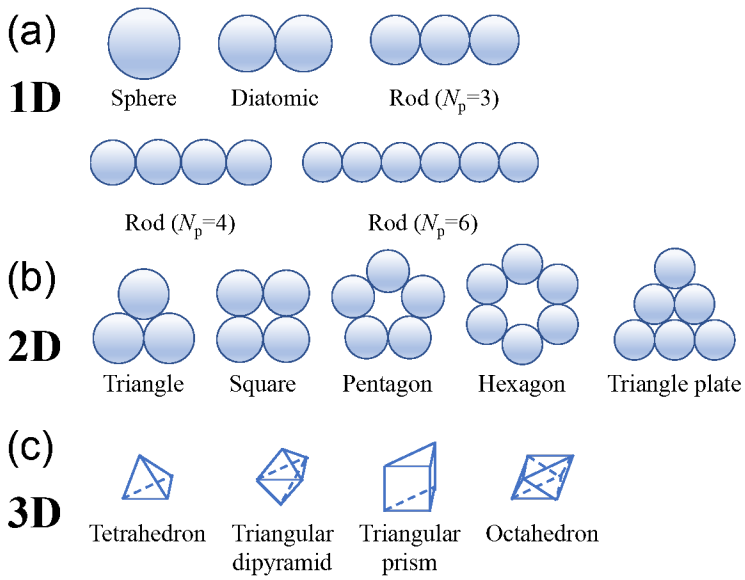

Fig.1. The three families of penetrant shapes studied. (a) linear (1D-like) rod model with $N_{\text{p}} = 1$ (spherical model), 2, 3, 4, 6. (b) Planar (2D-like) molecules including the triangle, square, pentagon, hexagon, and triangular plate. (c) Globular (3D-like) models including the tetrahedron, triangular dipyramid, triangular prism, and octahedron. The size of the elementary site is chosen such that the space filling volume of all different shaped penetrants is *identical*.

Table 1. Diameter of a single penetrant site in units of polymer monomer site diameter, d_{s}/σ, the single-molecule radius of gyration, $R_{\text{g}}/d_{\text{s}}$, and aspect ratio (measure of shape asymmetry) of the molecular penetrants defined as $\lambda = 2R_{\text{g}} + d_{\text{s}}$ in units of σ. The values listed in the parentheses corresponds to $d_{\text{eff}}/\sigma = 0.55$ systems, while those outside represent the $d_{\text{eff}}/\sigma = 0.8$ results.

penetrant shapes	**sphere**	**diatomic**	**rod ($N_{\text{p}} = 3$)**	**rod ($N_{\text{p}} = 4$)**	**rod ($N_{\text{p}} = 5$)**
d_{s}/σ	0.8 (0.55)	0.635 (0.436)	0.555 (0.381)	0.504 (0.346)	0.468 (0.322)
$R_{\text{g}}/d_{\text{s}}$	0	0.5	0.817	1.118	1.414
λ/σ	0.8 (0.55)	1.270 (0.873)	1.460 (1.004)	1.631 (1.121)	1.791 (1.231)
penetrant shapes	**rod ($N_{\text{p}} = 6$)**	**triangle**	**square**	**pentagon**	**hexagon**

d_s/σ	0.440 (0.303)	0.555 (0.381)	0.504 (0.346)	0.468 (0.322)	0.440 (0.303)
R_g/d_s	1.708	0.577	0.707	0.851	1
λ/σ	1.944 (1.337)	1.195 (0.822)	1.217 (0.836)	1.264 (0.869)	1.321 (0.908)
penetrant shapes	**triangle plate**	**tetrahedron**	**triangular dipyramid**	**triangular prism**	**octahedron**
d_s/σ	0.440 (0.303)	0.504 (0.346)	0.468 (0.322)	0.440 (0.303)	0.440 (0.303)
R_g/d_s	0.913	0.612	0.683	0.764	0.707
λ/σ	1.244 (0.855)	1.121 (0.771)	1.107 (0.761)	1.113 (0.765)	1.063 (0.731)

We study multiple examples of three classes of shaped penetrants (see Fig.1): (i) 1D-like rod models with $N_p = 1 - 6$ where $N_p = 1$ is the pure hard sphere model; (ii) 2D-like planar models including the triangle, square, pentagon, hexagon, and triangle plate; and (iii) 3D-like globular models including the tetrahedron, triangular dipyramid, triangular prism, and octahedron. All models adopt the tangent model (site diameter equals nearest neighbor bond distance) to calculate their intramolecular structure factor. To analyze the dynamics of BTBP and TBRb molecules and compare with experiment, we also study several other special non-tangent (overlapping site) models as discussed in Section VI-B.

To elucidate the explicit consequences of penetrant shape, we enforce that different penetrant shapes have the same space filling volume; for context we recall that our prior comparisons of theory and experiment suggests penetrant volume is often the leading order effect [25, 26, 29, 31]. Given we know [25-27, 31] that larger volume spherical penetrants behave very differently than their smaller analogs due to collective elastic effects on their activation barrier for hopping, we choose two different values of fixed penetrant volume corresponding to effective

diameters of $d_{\rm eff}/\sigma \equiv N_{\rm p}^{1/3} d_{\rm s}/\sigma = 0.8$ and 0.55, where $d_{\rm eff} \equiv (6V_{\rm p}/\pi)^{1/3}$ determines the size or volume $V_{\rm p}$ of a penetrant. For the larger one, based on prior work [27, 29, 31] on spherical penetrants and our present analysis, we expect that both the penetrant local cage and elastic barriers are crucial for some of the shaped penetrants studied, while for the smaller one the elastic barrier is expected to be negligible. Thus, we address the physics of molecular shape for "large" and "small" penetrants in the sense of the importance of collective elasticity on their activated hopping.

As a metric of penetrant shape (versus space filling volume), we adopt the classic radius of gyration given as $R_{\rm g} \equiv \sqrt{\frac{1}{2N_{\rm p}^2}\sum_{i,j}^{N_{\rm p}} d_{ij}^2}$, with d_{ij} the center-to-center distance between sites i and j within the same penetrant. As a measure of shape asymmetry, we define a "penetrant aspect ratio" as $\lambda/\sigma = (2R_{\rm g} + d_{\rm s})/\sigma$. Values of $R_{\rm g}/d_{\rm s}$ and λ/σ for the shapes shown in Fig.1 are presented in Table 1 for values of penetrant effective diameters studied, $d_{\rm eff}/\sigma = 0.8$ and 0.55.

B. Shape effects on the penetrant-polymer packing correlation function

Our core idea is the leading order effect of non-spherical shape is the change of penetrant-polymer packing at the elementary interaction site level of the real forces, and hence the kinetic constraints for penetrant motion. We describe the latter at a simplified center-of-mass (CM) trajectory level in analogy with how the dynamics of spherical penetrants are rigorously described. Thus, the explicit effect of rotational dynamics is ignored (treating this is in general an unsolved problem in the theory), a simplification that has had significant prior success work for the activated dynamics for one-component non-spherical molecular and colloidal fluids [47-50]. In this section, we briefly discuss representative examples of the penetrant-matrix packing structure, which provide physical insight for the dynamical results of subsequent sections. As discussed below and previously [28, 29, 40], since we assume the site-site packing structure of polymer melts to be the

same as that of polymer networks, we analyze only the cross radial distribution function of dilute penetrants in polymer melts.

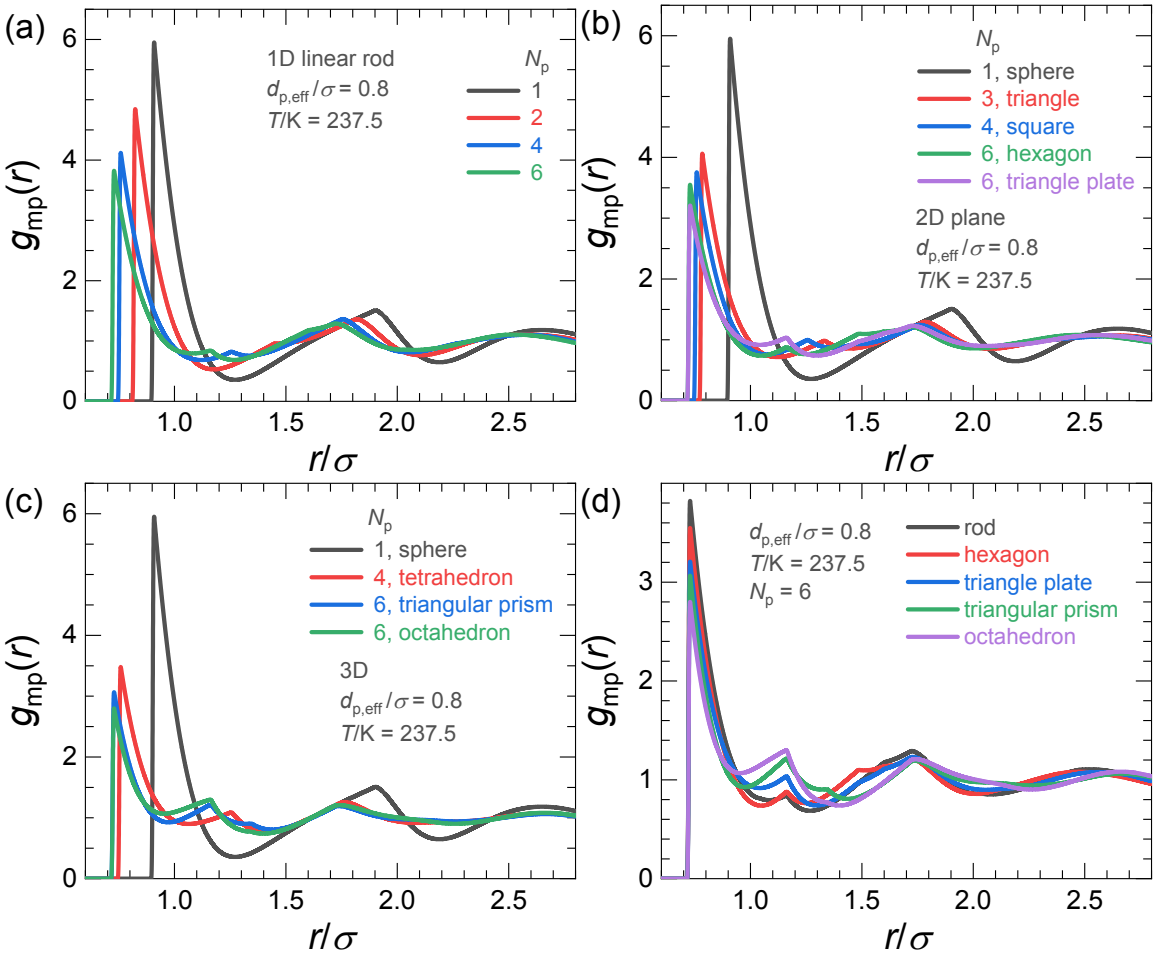

Fig.2: Penetrant − polymer site-site cross pair correlation function, $g_{\mathrm{mp}}(r)$, as a function of separation scaled by the polymer monomer diameter, using PRISM-PY theory for (a) 1D, (b) 2D, and (c) 3D shapes with the same molecular volume but different site numbers N_{p}. (d) Same display as in (a) to (c) but for all $N_{\mathrm{p}} = 6$ systems studied. The results shown are for a penetrant-to-matrix effective size ratio $d_{\mathrm{eff}}/\sigma = 0.8$ and a lower temperature ($T = 237.5\mathrm{K}$, very close to the PnBA melt glass transition temperature T_{g}) where the basic structural characteristics are more obvious relative to that for smaller size penetrants or high/medium temperatures.

Given the variability of polymer-molecule packing with penetrant shape is larger for the bigger penetrants, we present illustrative results for the cross pair correlation function, $g_{\mathrm{mp}}(r)$, of $d_{\mathrm{eff}} = 0.8$ systems (the trends for the $d_{\mathrm{eff}} = 0.55$ systems are similar and not shown). Figures 2a, 2b, and 2c show $g_{\mathrm{mp}}(r)$ of 1D, 2D, and 3D systems for penetrants of the same effective volume

but a different number of sites, respectively. Overall, one observes that for all non-spherical penetrants the contact value $g_{\mathrm{mp}}(d_{\mathrm{mp}})$ (where $d_{\mathrm{mp}} = \frac{d_s + \sigma}{2}$) and its location decrease with increasing N_{p} , as expected since the effective diameter for each site, $d_{\mathrm{s}} \equiv d_{\mathrm{eff}}/N_{\mathrm{p}}^{1/3}$, decreases when keeping the total penetrant volume the same. However, each penetrant contains several sites, and $N_{\mathrm{p}} g_{\mathrm{mp}}(d_{\mathrm{mp}})$ does increase as N_{p} grows. Since intermolecular forces on all sites of each molecule contribute to its CM dynamics, one can expect the total forces on each molecule will be larger when N_{p} is higher even if penetrant volumes are identical. As confirmed below, this increases the difficulty of penetrant hopping, and both the penetrant local cage and elastic barriers increase, and the penetrant jump distance decreases with N_{p}. We also find a weak peak beyond contact in the cross pair correlation function for all non-spherical systems, which arises from the connectedness (bonding) correlations of different sites in each molecule. As is well known from the classic theories of rigid molecular liquids [47-52], contact of a penetrant site with a monomer site determines the "contact value" $g_{\mathrm{mp}}(d_{\mathrm{mp}})$, but the other sites in the same tagged penetrant are constrained by bonding to be at a fixed distance from it leading to a weak peak at a distance modestly longer than d_{mp}. However, we emphasize that this effect is not important for our core dynamical results presented below.

For fixed $N_{\mathrm{p}} = 6$, several $g_{\mathrm{mp}}(r)$ for different shaped penetrants are also presented in Fig.2d. One sees that the contact value increases with aspect ratio (see Table 1). However, the value of the second weak peak *decreases* as the degree of asymmetry increases. These features suggest, at zeroth order, the penetrant relaxation time becomes smaller as the aspect ratio decreases. Finally, we note that the hexagon model is not maximally compact in that it contains a small void in its center that cannot be sterically accessed by polymer sites, which may have special consequences on its dynamics, as discussed below.

III. Dynamical Theories

We now briefly review the basic elements of the two dynamical theories employed: ECNLE theory for Kuhn segment relaxation in one-component polymer melts/networks [27, 35, 40], and SCCH theory for dilute penetrant dynamics for which ECNLE theory of pure polymer systems enters as input [27-29]. Additional background material is in the SI.

A. ECNLE theory for pure polymer melts and networks

As schematically indicated in the inset of Fig.3a, the polymer activated alpha relaxation process is described at the Kuhn segment scale corresponding to treating N_K (here equal to 8/3) connected beads as a rigid unit, with chain connectivity constraints dynamically ignored beyond the Kuhn scale [35, 37, 38, 40]. Full chain connectivity at the elementary site level is retained for all equilibrium correlations functions that enter the dynamical theory to quantify kinetic constraints. The foundational dynamical quantity is the Kuhn segment CM scalar displacement dependent dynamic free energy, $F_{\mathrm{dyn,K}}$ (inset of Fig.3b). At the high melt-like packing fractions of present interest, it has a localized form and a local cage barrier, $F_{\mathrm{B,K}}$. To achieve a sufficiently large particle hop (jump distance of Δr_{K}), particles or sites outside the nearest neighbor shell (defines the local "cage") must elastically displace in a collective manner by a small amount to create the required space for a large amplitude hop. This introduces as second contribution to the dynamic barrier called the elastic barrier $F_{\mathrm{el,K}}$. The total activation barrier is $F_{\mathrm{total}} = F_{\mathrm{B}} + F_{\mathrm{el}}$. This is the core physical idea of the ECNLE theory, corresponding to the alpha relaxation event being a coupled spatially local-nonlocal activated process. The magnitude of the elastic barrier and its dependence on thermodynamic state are controlled by the Kuhn segment jump distance Δr_{K} and harmonic curvature (or spring constant setting the energy scale for elastic fluctuations) $K_{0,\mathrm{K}}$, which are both predicted from the dynamic free energy and hence the structural packing correlations [33-35, 40].

The Kramers mean first passage time [53, 54] is adopted to compute the mean Kuhn segment hopping time ratio, $\tau_{\mathrm{hop,K}}/\tau_{\mathrm{s,K}}$, from which the mean Kuhn segment alpha time follows as $\tau_{\alpha,\mathrm{K}} = \tau_{\mathrm{s,K}} + \tau_{\mathrm{hop,K}}$, where $\tau_{\mathrm{s,K}}$ is the non-activated short length scale relaxation time [25, 34, 35] the formula for which is given elsewhere.[35, 40] To carry out quantitative calculations and compare with experiments, the elementary timescale of a Newtonian liquid, τ_0=16$\phi\sigma(\beta M/\pi)^{1/2}$ (typically of order ~ 1 ps [25, 38-40]) is selected as the time unit; this can be adjusted to reflect any system-specificity, but has a weak effect since it enters as a prefactor with typical values in the range of 0.1-10 ps [38, 39]. Figure 3a present the theoretical mean alpha time $\tau_{\alpha,\mathrm{K}}/\tau_0$, along with the experimental alpha time of a PnBA melt in units of ps [40]. As discussed previously [40], good agreement is found.

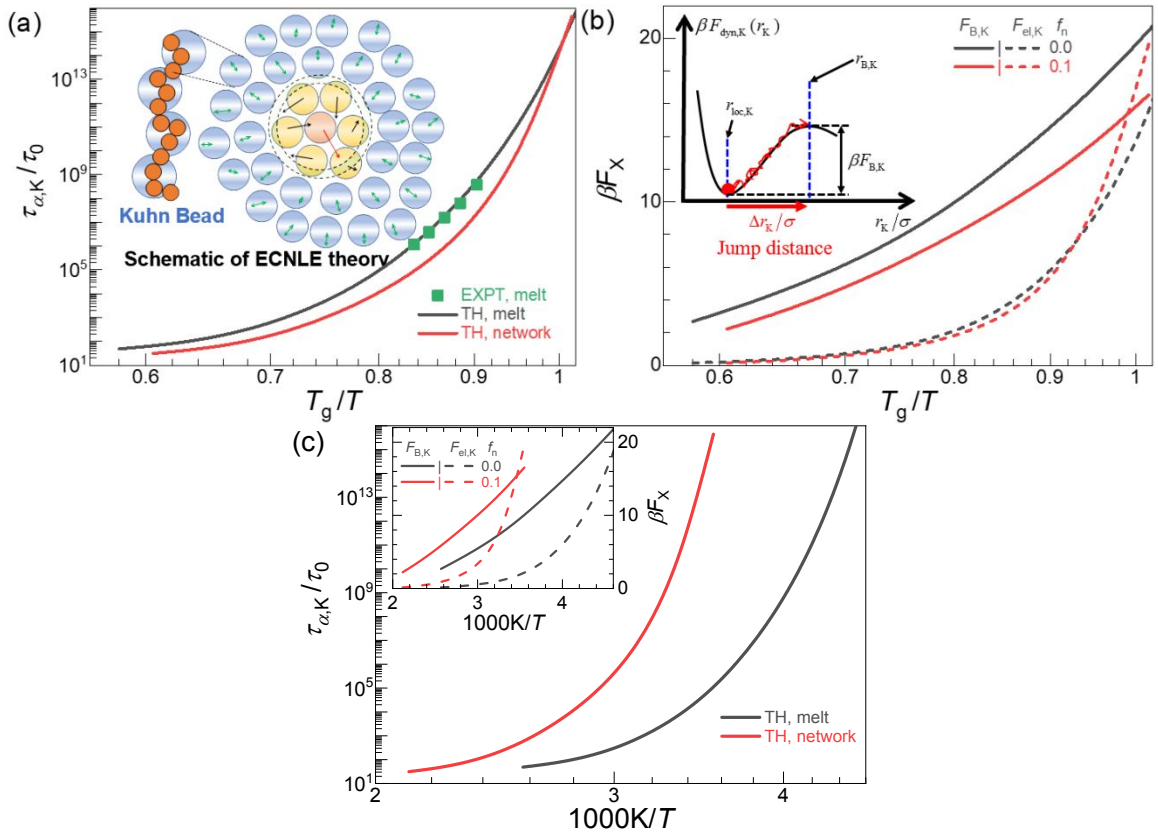

Fig.3. (a) Dimensionless polymer Kuhn segment mean alpha relaxation time $\tau_{\alpha,\mathrm{K}}/\tau_0$ as a function of T_g/T (Angell style plot) at two crosslink densities for the PnBA melt ($f_\mathrm{n} = 0$) and a heavily crosslinked network studied in experiments ($f_\mathrm{n} = 0.1$) [40]. The experimental alpha times [40] of the PnBA melt in picoseconds is also shown. The dynamically determined T_g from ECNLE theory is defined as requiring $\tau_{\alpha,\mathrm{K}}/\tau_0$ equals 10^{14} which corresponds to 100 s based on adopting $\tau_0 \approx 1$

ps, while the experimental T_g of the PnBA melt (226K) and network (286K) are determined based on the thermodynamic method [2, 40] using differential scanning calorimetry (DSC). Inset of (a) shows a schematic of the physical ideas of ECNLE theory, and the mapping of a polymer to a discrete chain of tangent bead (interaction sites) model that is described dynamically at the Kuhn segment scale. (b) Kuhn segment local cage and collective elastic barriers as a function of T_g/T at the two crosslink densities $f_n = 0$ and $f_n = 0.1$. The inset of (b) schematically illustrates the key features of the dynamic free energy as a function of Kuhn segment dimensionless displacement, and relevant length and energy scales are indicated. (c) Main and inset are the same theoretical results as in (a) and (b), respectively, but plotted as a function of 1000K/T.

For the crosslinked network, we previously [28, 29, 40] argued that at zeroth order chemical crosslinking does not change the site-site structural pair correlations. Hence, we adopt the previously validated [28, 29, 40] "neutral confinement" model defined as random pinning of a fraction of polymer sites to mimic the dynamical consequences of chemical crosslinking as a fraction [$f_n = n_{crosslink}/(n_{crosslink} + n_{monomer})$] of immobile segments that are distributed in a regular manner along a chain (see schematic in Fig.4). Here, $n_{crosslink}$ and $n_{monomer}$ are the interaction site (bare bead) level number of crosslinked (pinned) and normal mobile (unpinned) beads, respectively. In our prior study for the PnBA networks [40], the comparison between experiment and theory suggests that $f_n = 0.1$ corresponds to the most heavily crosslinked network. Thus, we focus mainly on the two extreme cases: the PnBA melt ($f_n = 0$) and the most heavily crosslinked network ($f_n = 0.1$). The dynamic free energy of Kuhn segments in networks was shown previously [40]. The calculated mean alpha time for the most heavily crosslinked network is also shown in Fig.3a. The fragility of the PnBA network is only modestly larger than that of its melt, and a near collapse in the Angell representation is predicted, consistent with experiment and simulation [40].

Figure 3b presents the local cage and elastic barriers for the PnBA melt and crosslinked network as a function of T_g/T. We note that the network T_g at $f_n = 0.1$ is 286K, significantly larger than that in melts (226K), consistent with experiment and simulation [40]. The difference in absolute values of the alpha times between PnBA melts and networks in the T_g/T representation of

Fig.3a is mainly due to a difference in their local cage barriers (see Fig.1b). Relative to the weak difference in the T_g/T dependence of the cage barriers (i.e., the slope) in the deeply supercooled regime, the T_g/T dependence of elastic barriers for PnBA melts and networks differs significantly, which is the origin of their modest difference of fragilities. Fig.3c shows the same alpha time and barrier results but now as a function of 1000K/T. The melt local cage barrier is smaller than that its network analog at a fixed temperature due to the higher T_g of the network, and the elastic barrier in the melt is far smaller than that of the network at a fixed temperature [28, 40]. These different temperature dependences of the Kuhn segment alpha time of polymer melts and crosslinked networks will have a significant consequence on penetrant dynamics as shown in section IV.

B. SCCH theory for shaped penetrants.

We briefly recall the key physical aspects of SCCH theory, originally formulated for dilute spherical penetrants [25, 26, 33]. The penetrant dynamics is of a coupled local-nonlocal activated hopping process. The novel aspect is that penetrant hopping is self-consistently coupled with an activated dynamic "facilitation displacement" of the Kuhn segments, the details of which are determined by the Kuhn segment dynamic free energy. Thus, the penetrant dynamic free energy depends on *both* the penetrant and Kuhn segment displacements (r_p and r_K), as schematically illustrated in Fig.4.

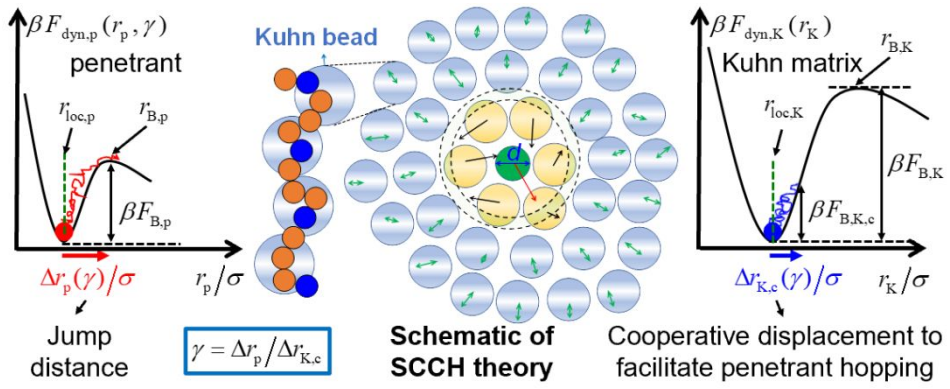

Fig.4. Schematic of the physical ideas of SCCH theory (shown for visual simplicity for a spherical particle system, the green bead is the penetrant) based on coupled dynamic free energies for the penetrant and Kuhn segment displacements (relevant length and energy scales are indicated) with a trajectory coupling parameter defined as $\gamma = \Delta r_{\mathrm{p}}(\gamma)/\Delta r_{\mathrm{K,c}}(\gamma)$. The introduction of crosslinks via the regular pinning of interaction sites along a polymer chain is also shown, where the blue beads represent the pinned monomers that mimic chemical crosslinks, while the orange beads are unpinned mobile monomers.

The mathematical formulation of SCCH theory has been discussed in great detail previously for a dilute spherical penetrant in a hard sphere fluid [25, 26, 33, 41] and also in a polymer melt [27] or network [28, 29]. The difference for *multi-site shaped* penetrants is technical and straightforward to formulate. It enters via the derivative of the penetrant dynamic free energy at the CM level which now has contributions from polymeric forces on all sites of the penetrant; see section II-C of the SI for technical details. At the dynamic free energy level, this is the only new feature when penetrant motion is described at the CM translation level. The explicit rotational dynamics of non-spherical penetrants is ignored (pre-averaged) to render the problem tractable, as previously done with significant success for 1-component molecular and colloidal fluids [47-50]. Generalization to explicitly treat coupled translation-rotation activated hopping is generally complex, though it has been achieved for the special geometry of uniaxial linear 1-component fluids [55, 56].

Finally, the penetrant alpha time is calculated as $\tau_{\alpha,\mathrm{p}} = \tau_{\mathrm{s,p}} + \tau_{\mathrm{hop,p}}$, where the characteristic short-time scale $\tau_{\mathrm{s,p}} = d_{\mathrm{eff}}^2/D_{\mathrm{s,p}}$ is slightly different from the previous work for spherical penetrants due to the influence of penetrant shape; see section II-C of the SI for technical details.

Semi-quantitatively, we estimate the penetrant hopping diffusion constant by using the Fick's law relationship as done previously, $D_{\mathrm{p}} = \frac{(\Delta r_{\mathrm{p}})^2}{6\tau_{\mathrm{hop,p}}}$.[25, 26, 57]. In the framework of SCCH theory for polymer melts, the penetrant diffusion constant is dominated by the variation of the activated

hopping rate ($1/\tau_{\mathrm{hop,p}}$) relative to small variations of the jump distance prefactor $(\Delta r_{\mathrm{p}})^2$ (see Fig.S5a). Hence, we emphasize that our discussion below of the penetrant relaxation time is directly germane to the corresponding diffusion constant. A key prediction of SCCH theory is that the temperature dependence of the penetrant relaxation time in the dilute limit of interest is dominated by the matrix[25]. In our recent work[31], we confirmed this prediction based on analyzing experimental penetrant diffusion constant data for selected chemically complex penetrants and molecular and polymer melt matrices. This provides objective support for the formula $D_{\mathrm{p}} = \frac{(\Delta r_{\mathrm{p}})^2}{6\tau_{\mathrm{hop,p}}}$ and the fact that $(\Delta r_{\mathrm{p}})^2$ plays a minor role in determining the temperature dependence of diffusion constant.

The relationship, $D_{\mathrm{p}} = \frac{(\Delta r_{\mathrm{p}})^2}{6\tau_{\mathrm{hop,p}}}$ works well for polymer melts, but for crosslinked polymer networks an additional contribution to the slowing down of penetrant mass transport can emerge due to geometric mesh confinement. This issue has been recently addressed in detail based on theory, experiment, and simulation [28-30]. The relationship between the penetrant relaxation time and diffusion constant was proposed to be $D_{\mathrm{p}} = f(C)\frac{(\Delta r_{\mathrm{p}})^2}{6\tau_{\mathrm{hop,p}}}$, where $f(C)$ represents the mesh confinement effect that only depends on the confinement parameter C defined as the ratio of the penetrant diameter to mean mesh diameter which is a function solely of crosslink density. At a fixed mesh confinement, $f(C)$ behaves as a constant when studying the temperature dependence of penetrant diffusion or relaxation, and hence the temperature dependence of D_{p} is expected to be the same as that of its inverse relaxation or hopping time, the same situation as in melts. When focusing on crosslinking effects at fixed temperature, we have recently confirmed based on experiment and simulation results [29] that $f(C)$ behaves (surprisingly) as an exponential function with $\mathrm{T_g}(f_{\mathrm{n}})/T$. This is effectively the same dependence as that of the inverse penetrant relaxation

time, with differences only entering via prefactors [29]. Moreover, quantitatively the entropic mesh confinement effect on penetrant diffusivity for penetrants of typical size (even the relatively large aromatic dye molecules [29]) is a perturbation relative to the reduction of the polymer alpha relaxation rate which is the leading order effect on penetrant dynamics implying $D_{\rm p} \propto \frac{1}{\tau_{\rm hop,p}} \approx \frac{1}{\tau_{\alpha,\rm p}}$. This finding motivates the neglect of the 2nd order explicit mesh confinement effects in our present study. Furthermore, we emphasize that dielectric experiments[2, 31] and simulations[30] have shown that the penetrant alpha relaxation time can be directly measured. Thus, for all the above reasons, we consider below mainly the penetrant relaxation time, where the found conclusions should also be applicable to inverse diffusion constant of the penetrant.

IV. Shape Effects on the Penetrant Alpha Relaxation Time

In this section we study how the penetrant alpha time is affected by its shape at fixed penetrant space filling volume over a wide range of temperatures and crosslink densities in PnBA systems for two choices of penetrant molecular volumes (representative of "small" and "large"). We also discuss the physical mechanism underlying shape effects in the theory, and propose a specific variable to organize the dynamical consequences of penetrant shape.

A. Shape effects in absolute temperature space

We first analyze the shape effects on the penetrant alpha time $\tau_{\alpha,\rm p}$ in units of the elementary timescale τ_0 (of order ~1 ps in typical experiments) in absolute temperature space, i.e., as a function of $1000{\rm K}/T$. Figures 5a, 5b, and 5c presents calculations of $\tau_{\alpha,\rm p}/\tau_0$ for 1D, 2D, and 3D like shaped penetrants in both polymer melts and networks at fixed effective penetrant diameter $d_{\rm eff}/\sigma = 0.8$ where collective elastic effects on penetrant hopping are relatively important. One sees from Fig.5a for rod-like penetrants that the temperature dependence of $\tau_{\alpha,\rm p}/\tau_0$ in melts changes significantly

with N_{p}, increasing by ~5 decades at the lowest temperature studied when varying N_{p} from 1 to 6. However, the temperature dependence of $\tau_{\alpha,\mathrm{p}}/\tau_0$ for the more globular 3D systems (Fig.5c) varies only a very small amount. We view this as a natural consequence of the studied 3D shapes being relatively globular and hence roughly isotropic and sphere-like (see Table 1, their aspect ratios λ are all very close to that of sphere).

For 2D-like planar penetrants (Fig.2), the variability of $\tau_{\alpha,\mathrm{p}}/\tau_0$ with specific shape is intermediate between that exhibited by the 1D and 3D systems. Specifically, the alpha times vary by ~2.5 decades total at the lowest temperature studied.

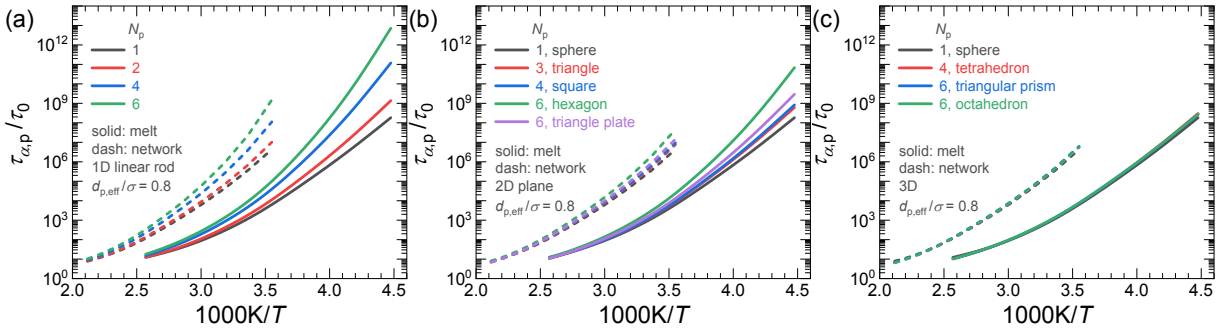

Fig.5. Alpha relaxation time of shaped penetrants, $\tau_{\alpha,\mathrm{p}}/\tau_0$, for $d_{\mathrm{eff}}/\sigma = 0.8$ in a polymer melt (solid) and crosslinked network (dash) as a function of inverse temperature $1000\mathrm{K}/T$ over a wide range of penetrant shapes but of identical space filling volume: (a) 1D, (b) 2D, and (c) 3D shapes.

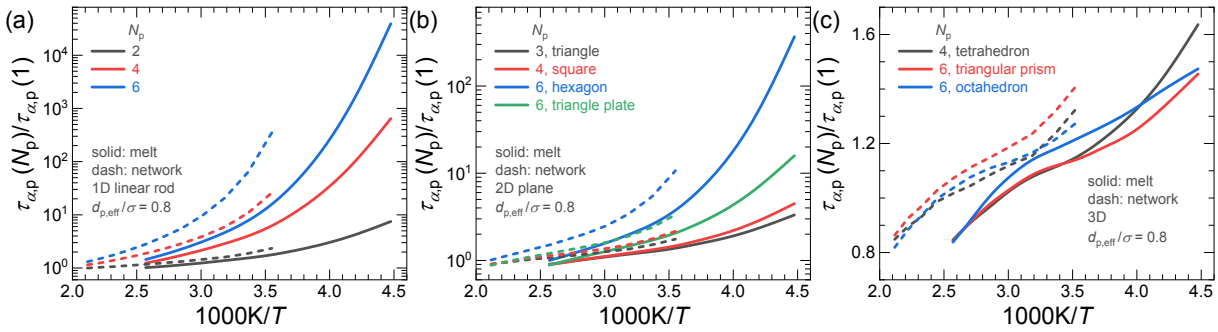

Fig.6. Ratio of penetrant alpha time of different shapes but identical volume ($d_{\mathrm{eff}}/\sigma = 0.8$) compared to a spherical penetrant, $\tau_{\alpha,\mathrm{p}}(N_{\mathrm{p}})/\tau_{\alpha,\mathrm{p}}(1)$, in a polymer melt (solid) and crosslinked network (dash) as a function of inverse temperature $1000\mathrm{K}/T$ for (a) 1D, (b) 2D, (c) 3D shapes.

As a general trend in Fig.5, at fixed temperature we predict $\tau_{\alpha,\mathrm{p}}/\tau_0$ in melts is always much lower than that in networks, as expected since crosslinking slows down segmental relaxation

significantly thereby strongly affecting penetrant dynamics. [28-30]. To analyze the net influence of crosslinking on shape effects, we show in Fig.6 the ratio of the penetrant alpha time $\tau_{\alpha,\mathrm{p}}$ of different shapes to that of the corresponding same volume spherical penetrant, $\tau_{\alpha,\mathrm{p}}(N_\mathrm{p})/\tau_{\alpha,\mathrm{p}}(1)$. One sees that in over the same temperature range, the thermal dependence of penetrant relaxation in melts is less sensitive to its shape relative to that in networks for all penetrant shapes.

B. Shape effects in T_g/T space

From a basic scientific perspective, analysis of the penetrant relaxation time in reduced T_g/T space is also of interest, especially with regards to the role of crosslinking in networks compared to melts. Figure 7 shows results for all the $\tau_{\alpha,\mathrm{p}}/\tau_0$ data in Fig.5 but now plotted versus T_g/T. We find that within the wide range of $0.6 < T_\mathrm{g}/T < 1.0$, the temperature dependent trends of $\tau_{\alpha,\mathrm{p}}/\tau_0$ remains unchanged relative to the above analysis in $1000\mathrm{K}/T$ space for different shaped penetrants, i.e., relaxation times are ordered as 1D > 2D > 3D. The reason is simply that T_g is a constant and does not change the temperature dependence. However, for polymer melts and networks, their T_g values are significantly different and thus within the same T_g/T range, the relative temperature dependence of the penetrant relaxation time must be different from that observed in the same absolute temperature ($1000\mathrm{K}/T$) space. As shown in Fig.7, at the same degree of supercooling, i.e., at fixed T_g/T, $\tau_{\alpha,\mathrm{p}}/\tau_0$ in polymer melts is higher than that in networks, which is opposite to the trend observed in Fig.5 at a fixed temperature.

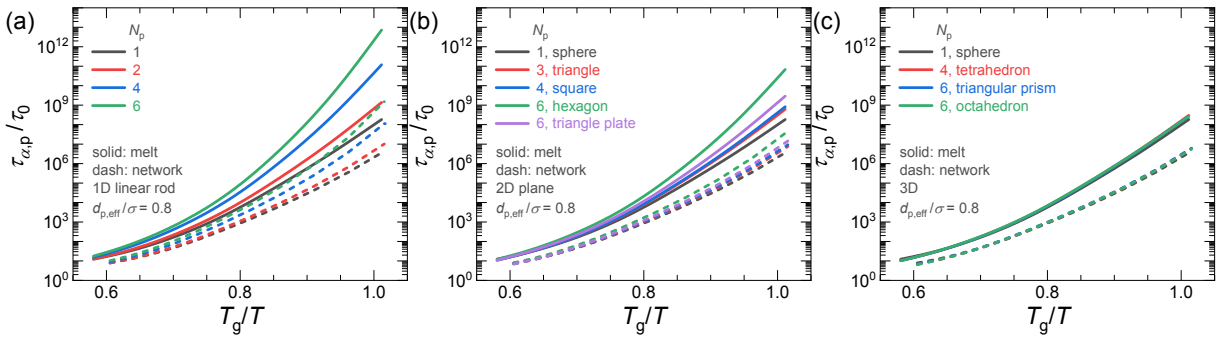

Fig.7. Same displays as in Fig.5 for the penetrant alpha time of different shapes, $\tau_{\alpha,\mathrm{p}}/\tau_0$, at $d_{\mathrm{eff}}/\sigma = 0.8$ in a polymer melt (solid) and crosslinked network (dash), but now plotted in the Angell representation, i.e., as a function of T_{g}/T, for (a) 1D, (b) 2D, and (c) 3D penetrant shapes.

Since crosslinked networks have a modestly larger fragility relative to melts [40], they have a lower Kuhn segment alpha time (see Fig.3a) at a fixed degree of supercooling. Assuming at the same T_{g}/T (< 1.0) the degree of trajectory coupling of penetrants and Kuhn segments is identical, then the weaker Kuhn segment relaxation rate must result in a smaller $\tau_{\alpha,\mathrm{p}}/\tau_0$ for the crosslinked network. This trend is reinforced by the fact the theory predicts that dynamical coupling between penetrants and Kuhn segments is smaller at fixed T_{g}/T for the crosslinked network than in the polymer melts as discussed below.

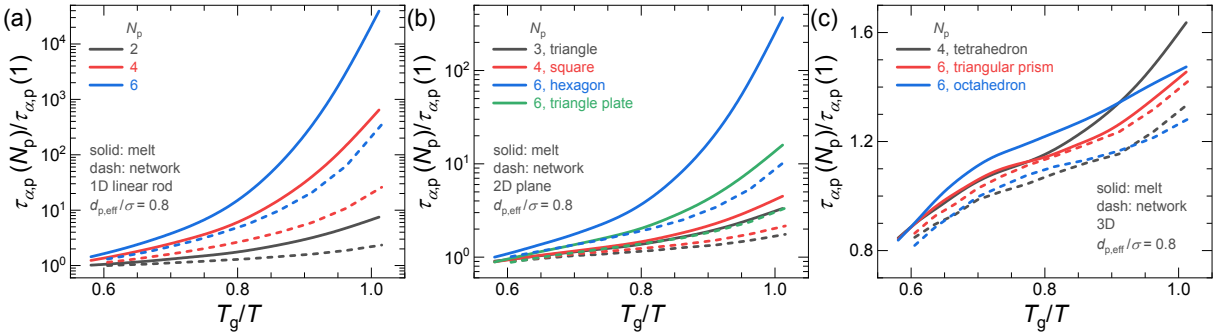

Fig.8. Same displays as in Fig.6 for the ratio of the penetrant alpha time for different shapes relative to that of a spherical shape, $\tau_{\alpha,\mathrm{p}}(N_{\mathrm{p}})/\tau_{\alpha,\mathrm{p}}(1)$, at $d_{\mathrm{eff}}/\sigma = 0.8$ in a polymer melt (solid) and crosslinked network (dash), but now plotted as a function of T_{g}/T for (a) 1D, (b) 2D, and (c) 3D penetrant shapes.

The ratio $\tau_{\alpha,\mathrm{p}}(N_{\mathrm{p}})/\tau_{\alpha,\mathrm{p}}(1)$ as a function of T_{g}/T is shown in Fig.8 for both the 1D, 2D, and 3D like penetrants (analog of Fig.6). Opposite to the temperature dependence at fixed absolute temperature ($1000\mathrm{K}/T$) range, the temperature dependence in melts over the same T_{g}/T range is more sensitive to penetrant shape than that in networks for all systems studied.

C. Physical mechanism of shape effects

In order to clarify the rich behavior discussed in the previous two sub-sections, we now dissect our numerically obtained results based on an analysis of all the theoretical elements that

underlie the calculation of the penetrant alpha time. If the reader is not interested in this detailed theoretical analysis, they can skip to sub-section IV-D. Given the similarities in both the $1000\mathrm{K}/T$ and T_g/T space representations of the temperature dependence of penetrant alpha times or barriers, we only discuss the barriers in the T_g/T representation.

The underlying physical origin of the predicted trends emerges from the behavior of the penetrant local cage and elastic barriers which are shown as function of T_g/T in Fig.9. Results are shown only for the case of larger penetrants which are strongly coupled to matrix motions, which have major contributions to their activation barrier from both the local cage and elastic barriers.

Figs.9a, 9b, and 9c show that the temperature dependence of local cage barriers is nearly identical for all penetrant shapes. This major finding establishes that the slope change in logarithmic alpha time versus inverse temperature (see Fig.5 and Fig.7) plots in the deeply supercooled regime arises almost entirely from the collective elastic barriers. This is further confirmed in Figs.9d, 9e, and 9f where we find the temperature dependence of the elastic barriers behave significantly different as penetrant shapes change. Moreover, it is remarkable that the nearly identical temperature dependence of the local cage barriers for different shaped penetrants of identical space filling volume suggests a type of dynamical averaging of shape on the time scale of penetrant hopping and relaxation. In fact, previously it has been shown that SCCH theory for spherical penetrants predicts a surprising factorization of the temperature and size ratio dependences of the penetrant activation barrier and alpha time [25, 31]. This prediction has been confirmed in experiments on chemically complex dilute penetrants in diverse molecular and polymeric liquids[31], suggesting that a type of shape averaging exists on long-time scales. Thus, our finding in Figs.9a-9c of a nearly identical temperature dependence of local cage barriers

confirms theoretically that shape averaging does exist on the time scale of penetrant hopping and long-time diffusion in matrices explicitly modeled as polymer melts and crosslinked networks.

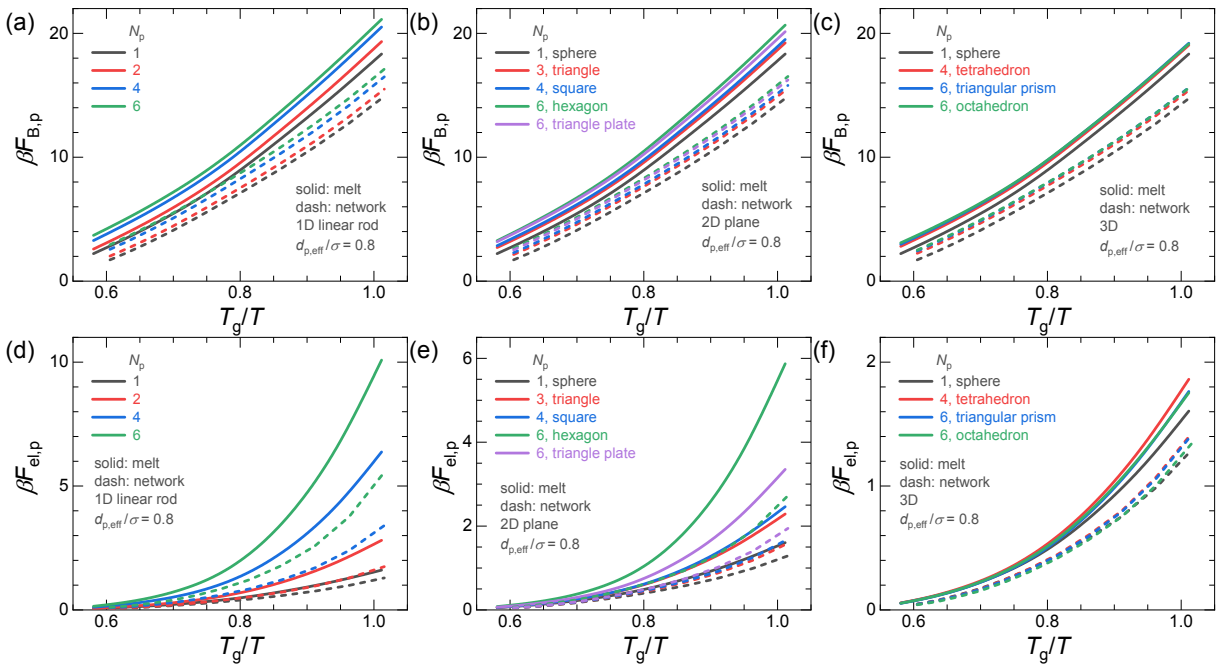

Fig.9. Penetrant local cage (a, b, c) and elastic (d, e, f) barriers (in units of thermal energy) as a function of T_g/T for the melt $f_n = 0$ (solid) and a heavily crosslinked network of $f_n = 0.1$ (dash) over a wide range of penetrant shapes having the same effective molecular volume for (a, d) 1D, (b, e) 2D, and (c, f) 3D penetrant shapes.

The absolute values of the dynamic barriers is also of interest. At high temperatures, the penetrant elastic barrier is negligible since its jump distance and the relative stiffness of the polymer matrix are small. Thus, the variation of the penetrant relaxation time for different penetrants at high temperatures arises mainly from local cage barriers. However, as seen in Fig.9, the elastic barrier does change significantly in the deeply supercooled regime, to a degree that depends significantly on penetrant shape which is far larger than that of local cage barriers. This suggests the difference of absolute value of the penetrant relaxation time for different shaped penetrants at low temperatures is attributed mainly to the elastic barriers, a crucial insight for the difficult problem of selective transport based on penetrant shape at fixed space filling volume.

Concerning the effect of network crosslinking, one observes in Figs.9a, 9b, and 9c that changes of the temperature dependence of local cage barriers is very limited with crosslinking over the whole range of T_g/T studied (only a slight decrease in slope for the network results relative to that of melts). Moreover, the difference in absolute value due to penetrant shape effects remains nearly of the same magnitude for networks and melts, although within the same T_g/T range the absolute value of the penetrant local cage barrier in networks is less than that in melts by a factor of ~4. Just like the cage barrier, the penetrant elastic barriers (see Figs.9d, 9e, and 9f) for melts are also higher in absolute value than in networks over all the range of T_g/T studied (in the $1000\mathrm{K}/T$ space, an opposite conclusion is obtained as discussed above for the alpha times). However, the difference between penetrant elastic barriers in melts and networks varies with temperature and penetrant shape, i.e., the temperature dependence of elastic barriers changes significantly with crosslinking and penetrant shape, in a manner that is different from the behavior of penetrant local cage barriers. We note for the 3D shapes studied, they are compact and roughly isotropic, and hence sphere-like, which delivers the negligible shape effects observed in Fig.9f.

D. Influence of penetrant size on shape effects

A striking prior prediction of SCCH theory for dilute hard spheres in a hard sphere matrix is that when the penetrant diameter is large enough, both the elastic and local cage barriers are important, while only the latter is important if the penetrant is "small enough" ($d_{\mathrm{eff}}/\sigma < 0.5$).[25, 26, 31] When the hard sphere matrix is replaced with polymers, the penetrant elastic barrier becomes quantitatively less important due to chain connectivity effects, and the crossover boundary between these two behaviors increases from d_{eff}/σ ~0.5 to ~0.6-0.7.[29] In above work we focused on $d_{\mathrm{eff}}/\sigma = 0.8$ which is greater than the crossover value, and hence both local cage and elastic barriers are important, particularly for some shaped penetrants like rods with high values of N_p. Here, in

order to explore penetrant size effects, we study examples for smaller penetrant volume corresponding to $d_{\text{eff}}/\sigma = 0.55$ where only local cage barriers are important and the elastic barrier is negligible.

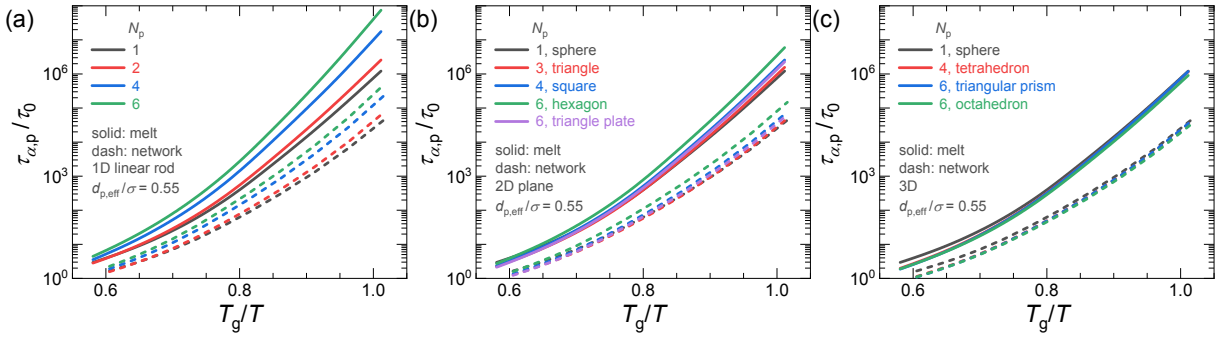

Fig.10 Same displays as in Fig.7 but for smaller penetrant size, $d_{\text{eff}}/\sigma = 0.55$: Alpha relaxation time of penetrant of different shapes, $\tau_{\alpha,\text{p}}/\tau_0$, at $f_{\text{n}} = 0$ (solid) and $f_{\text{n}} = 0.1$ (dash) as a function of T_{g}/T for (a) 1D, (b) 2D, and (c) 3D penetrant shapes.

Figures 10a, 10b, and 10c present results for $\tau_{\alpha,\text{p}}/\tau_0$ at $d_{\text{eff}}/\sigma = 0.55$ in both melts and networks for 1D, 2D, and 3D like penetrants, respectively. Relative to the significant changes discussed above for larger size penetrant ($d_{\text{eff}}/\sigma = 0.8$), changes with penetrant shape of the temperature dependence of $\tau_{\alpha,\text{p}}/\tau_0$ (i.e., the slope) are very limited for $d_{\text{eff}}/\sigma = 0.55$, a trend that physically arises due to the dominance of local cage barriers. We do observe a slight change of the temperature dependence with variable penetrant shape due to its influence on the relatively small penetrant elastic barriers. Finally, for much smaller penetrants $d_{\text{eff}}/\sigma < 0.5$, we find (not shown) the temperature dependence (the slope) of $\tau_{\alpha,\text{p}}/\tau_0$ with penetrant shapes does not change since the elastic barrier is always close to zero even for the $N_{\text{p}} = 6$ rod model.

Upon crosslinking, the $d_{\text{eff}}/\sigma = 0.55$ results broadly behave qualitatively the same as the corresponding$d_{\text{eff}}/\sigma = 0.8$ results: (i) the absolute value of $\tau_{\alpha,\text{p}}/\tau_0$ and the net impact of crosslinking on the shape effects in $\tau_{\alpha,\text{p}}/\tau_0$ for the polymer melts is larger than that of crosslinked networks within the same range of T_{g}/T studied; and (ii) the absolute value of $\tau_{\alpha,\text{p}}/\tau_0$ and the net

impact of crosslinking on the shape effects in $\tau_{\alpha,\mathrm{p}}/\tau_0$ for the same range of absolute temperature (or $1000\mathrm{K}/T$), however, is smaller or less obvious for the polymer melts than the crosslinked networks (see results for $\tau_{\alpha,\mathrm{p}}/\tau_0$ at $d_{\mathrm{eff}}/\sigma = 0.55$ in the $1000\mathrm{K}/T$ space in Fig.S1).

E. Shape effects on the exponential relationship between penetrant alpha time and crosslink density

Recently, we [28, 29] and our simulation collaborators [30] found an exponential relationship between the penetrant alpha time and $T_{\mathrm{g}}(f_{\mathrm{n}})/T$ (the variable here is crosslink fraction, f_{n}) at various fixed temperatures for dilute spherical penetrants in crosslinked networks. One may wonder if this exponential relationship continues to hold for the activated transport of shaped penetrants. Based on SCCH theory as previously applied to PnBA polymer networks of variable crosslink density [28, 29], we calculate the penetrant alpha times of three shaped models (sphere, hexagon, and rod with $N_{\mathrm{p}} = 6$) over the same wide range of f_{n} studied previously. Figure 11 shows $\tau_{\alpha,\mathrm{p}}/\tau_0$ as a function of the crosslinking dependent glass transition temperature $T_{\mathrm{g}}(f_{\mathrm{n}})/T$ for the $d_{\mathrm{eff}}/\sigma = 0.55$ and 0.8 models at three fixed temperatures spanning the weakly to strongly supercooled regimes. For *all* penetrant shapes, both effective penetrant sizes, and fixed temperatures studied, the linear relationship between $\log(\tau_{\alpha,\mathrm{p}}/\tau_0)$ and $T_{\mathrm{g}}(f_{\mathrm{n}})/T$ remains qualitatively *unchanged*. Moreover, for the small penetrants, the slope even remains essentially identical for different shapes, indicating a significant degree of dynamical shape averaging. The physical reason this occurs is that only the penetrant local cage barrier is important and its temperature dependent changes with penetrant shape are highly limited, per the discussion above. On the other hand, for the larger penetrant, both local cage and elastic barriers are crucial, and the latter is more significantly affected by penetrant shape. This results in an increased slope of the $\log(\tau_{\alpha,\mathrm{p}}/\tau_0)$ versus $T_{\mathrm{g}}(f_{\mathrm{n}})/T$ plot as the penetrant shape changes from sphere to hexagon to a 6-site

rod, as shown in Fig.11b in the deeply supercooled regime where the elastic barrier is relatively large. Additionally, at intermediate or high temperatures, the elastic barrier is not important and the local cage barrier again dominates, and thus the slope of the exponential relationship between penetrant alpha time and $T_g(f_n)/T$ are all similar regardless of the penetrant size.

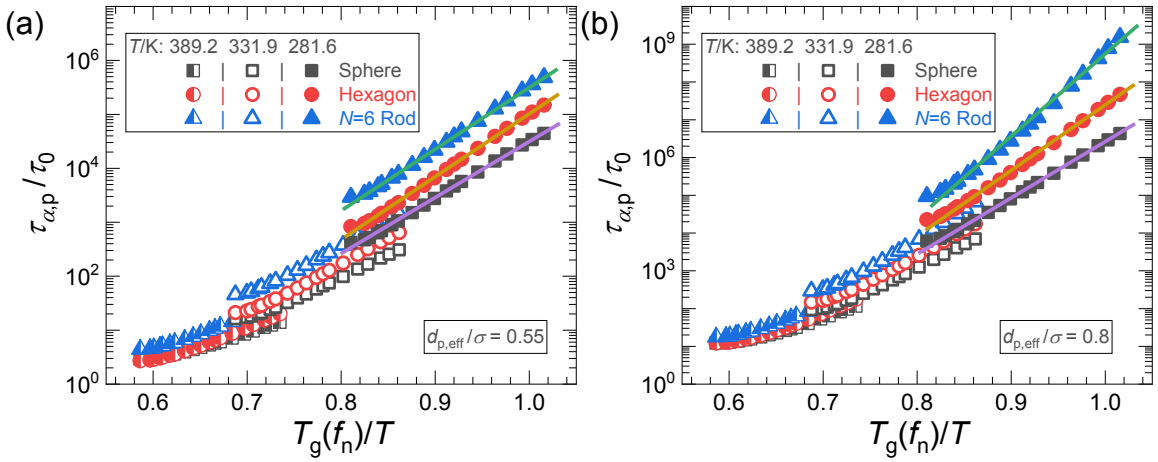

Fig.11 Penetrant mean alpha relaxation time in PnBA polymer networks of variable degree of crosslinking as a function of $T_g(f_n)/T$ at various fixed temperatures and for three penetrant shapes (sphere, hexagon, and $N_p = 6$ rod) with d_{eff}/σ equal to (a) 0.55 and (b) 0.8, respectively. Note that the changing variable in $T_g(f_n)/T$ is $T_g(f_n)$ and hence f_n, not the temperature.

We note that if one vertically shifts down the data of $\tau_{\alpha,p}/\tau_0$ in Fig.11 for the two lower temperatures (331.9K and 281.6K) by separate multiplicative factors, a data collapse onto a master curve can be obtained for each shape (see Fig.S2). However, the required empirical shift factor is different from the short-time scale τ_s, and does not seem to have a clear physical interpretation. Nevertheless, the ability to create a master curve is likely of practical experimental interest.

F. Combined variable to organize the effect of shape on dynamical selectivity

The above results have documented the importance of penetrant shape on their dynamics. A natural question is can one identify a single variable to organize shape effects on the penetrant relaxation time and hence diffusivity? The answer is likely not unique, but we have explored the

aspect ratio or degree of asymmetry variable $\lambda/\sigma = (2R_g + d_s)/\sigma$ as a possible candidate. In this section, we study whether λ/σ can organize the penetrant alpha times of different shapes.

Figure 12a shows the penetrant alpha time as a function of λ/σ for all the shapes studied above (including several 3- and 5-site models not discussed above) at fixed T_g/T and $d_{eff}/\sigma = 0.8$. We find the alpha times can be organized very well according to the value of λ/σ: when λ/σ is low (smaller than ~1.5 d_{eff}/σ), a plateau appears, and with further increase of λ/σ the penetrant alpha time grows exponentially. We view this finding as a minimal quantification of isochoric molecular shape-selectivity. Note that at fixed T_g/T, the penetrant shape selectivity is stronger in melts than in networks, particularly at low temperatures, a prediction relevant to the design of separation membrane materials. Consistent with Figs.7 and 8 that at fixed T_g/T the penetrant alpha time in networks are always smaller than in melts, Fig.12a shows that crosslinking does not modify the exponential increase of penetrant alpha time with aspect ratio in the large λ/σ regime, nor the critical value of λ/σ (~1.5 d_{eff}/σ) that separates the plateau and exponential increase regimes.

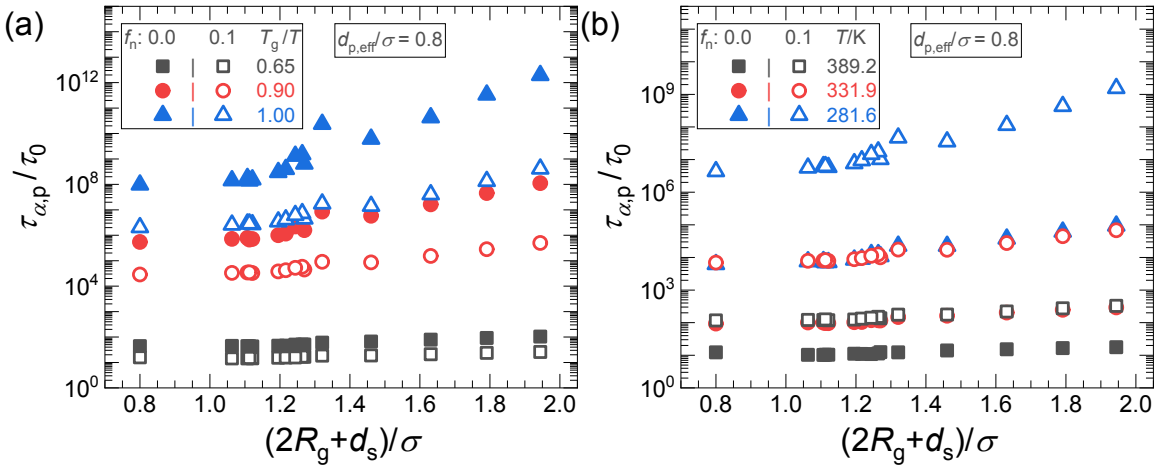

Fig.12. Penetrant relaxation time as a function of the dimensionless aspect ratio $\lambda/\sigma = (2R_g + d_s)/\sigma$ at (a) fixed T_g/T and (b) fixed inverse temperatures in both a polymer melt (solid symbols) and heavily crosslinked network (open symbols) over a wide range of penetrant shapes and temperatures for $d_{eff}/\sigma = 0.8$. From the left to right, the penetrant shapes are sphere, octahedron, triangular dipyramid, triangular prism, tetrahedron, triangle, square, triangle plate, pentagon, rod $N_p = 2$ rod, hexagon, $N_p = 3$ rod, $N_p = 4$ rod, $N_p = 5$ rod, and $N_p = 6$ rod.

If one considers the problem in fixed temperature space, we find the plateau and exponential behaviors remain unchanged (see Fig.12b), although the penetrant alpha time in networks becomes larger than that in the analogous melts, consistent with the findings in Figs.5 and 6. We note the slight deviation of the hexagon data in Fig.12 from the master curve is attributed to the fact that it has a small "hole" in its center that is not sterically accessible by polymer monomers which leads to some increase of its occupied volume and hence alpha time. Although different geometry-based ways can be envisioned to define the volume of a shaped molecule such that the "hole" effect (e.g., for a hexagon) can be better accounted for (e.g., inaccessible vs accessible volume of a penetrant to a polymer bead), its determination is a complex, system-specific, and non-unique task. Hence, we have adopted the simplest and most straightforward approach to define the penetrant molecular volume based on the space filling volume of interaction sites.

For the smaller penetrant systems ($d_{\text{eff}}/\sigma = 0.55$) our conclusions remain the same (see Fig.S3), including the critical value of λ/σ in distinguishing the plateau and exponential increase regime occurring at ~ 1.5 d_{eff}/σ.

We hope the proposed organizing variable $(2R_{\text{g}} + d_{\text{s}})/\sigma$ is of value in designing future experiments and in membrane applications to achieve better penetrant shape selectivity at fixed molecular volume. Finally, we note that the defined aspect ratio $\lambda = 2R_{\text{g}} + d_{\text{s}}$ includes not only the radius of gyration R_{g} , but also the site diameter d_{s}. We have checked that adopting either variable separately cannot organize the shape effects on penetrant diffusion selectivity numerically predicted by the theory.

V. Shape Effects on Decoupling of Penetrant and Polymer Dynamics

We now consider penetrant shape effects on the degree of dynamic decoupling between penetrants and Kuhn segments. We first consider the ratio of the alpha times of the penetrant and Kuhn segment, which is measurable in simulations and experiments. In search of a mechanistic understanding, we then analyze the difference between a Kuhn segment displacement *at* the penetrant and *at* Kuhn segment alpha times, $r_{\mathrm{K}} - r_{\mathrm{K,c}}$, and the trajectory coupling parameter, γ.

A. Alpha time ratio of penetrant to Kuhn segment

As previously studied using SCCH theory for dilute hard spheres in a hard sphere fluid [25, 26, 41], polymer melts [27] and networks [28, 29], the alpha time decoupling ratio $\tau_{\alpha,\mathrm{p}}/\tau_{\alpha,\mathrm{K}}$ is especially sensitive to collective elasticity effects given that the hopping of penetrants and Kuhn segments couples to this longer-range effect in a highly system-specific manner. In prior work [25, 27, 41], $\tau_{\alpha,\mathrm{p}}/\tau_{\alpha,\mathrm{K}}$ was plotted as a function of matrix packing fraction (analog of inverse temperature via the *T*-density mapping [36-39]) and $T_{\mathrm{g}}(f_{\mathrm{n}})/T$, and a weakly non-monotonic behavior was predicted. Specifically, the alpha time ratio initially increases slightly in the weakly supercooled regime which corresponds to high temperature or low crosslink density regimes where barriers are rather small and the non-activated short time dynamical process timescale τ_{s} matters. Upon entering the deeply supercooled regime, $\tau_{\alpha,\mathrm{p}}/\tau_{\alpha,\mathrm{K}}$ dramatically decreases indicating a strong decoupling between penetrant and matrix activated dynamics when the barriers become larger and dominate the alpha time. In the deeply supercooled regime, the crucial physical effect is the very different rate at which the penetrant and matrix elastic barriers grow with increasing the degree of supercooling, a difference significantly larger than that for their local cage barrier analogs.

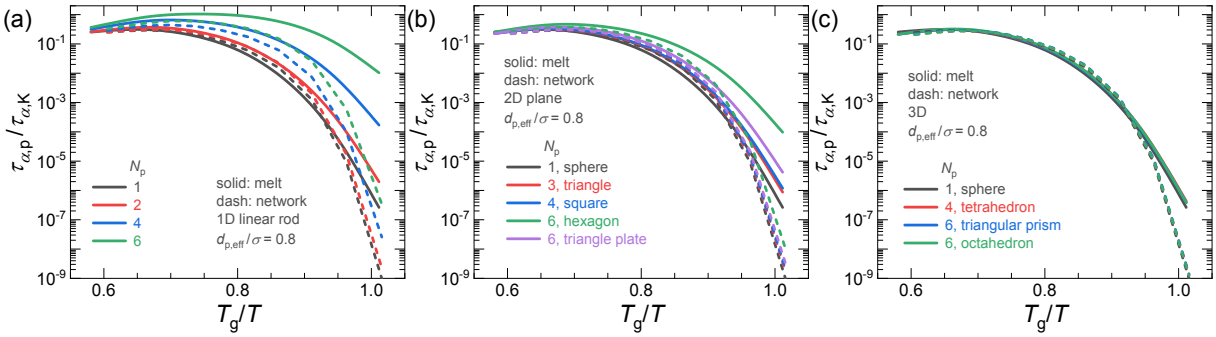

Fig.13. Degree of coupling between penetrant and Kuhn alpha relaxation times quantified by the ratio, $\tau_{\alpha,\mathrm{p}}/\tau_{\alpha,\mathrm{K}}$, as a function of T_g/T for $d_\mathrm{eff}/\sigma = 0.8$ in the polymer melt (solid) and heavily crosslinked network (dash) for various (a) 1D, (b) 2D, and (c) 3D penetrant shapes.

Figures 13a, 13b, and 13c show our theoretical predictions for the decoupling time ratio plotted versus T_g/T for $d_\mathrm{eff}/\sigma = 0.8$ for 1D, 2D, and 3D like molecular penetrants, respectively, in both polymer melts and crosslinked networks. The results span a wide range of T_g/T values from the rubbery regime, through the deeply supercooled regime, down to the kinetic glass transition. One observes that for all shapes the time ratio behaves weakly nonmonotonically with the degree of supercooling parameter, T_g/T, qualitatively consistent with the previous results for spherical penetrants [25, 27, 28, 41]. In the rubbery regime, tiny differences are observed for different shapes, while in contrast, in the deeply supercooled regime the time ratio exhibits significant differences with penetrant shape. By comparing the Kuhn segment barrier for the pure polymer in Fig.3b with the penetrant barriers in Fig.9, one can conclude that the local cage barrier for all shaped penetrants is not far from its Kuhn analog in the deeply supercooled regime. On the other hand, the absolute values of penetrant elastic barriers and their differences from the Kuhn segment analog are significantly dependent on penetrant shape. This provides the physical reason for the significant differences of $\tau_{\alpha,\mathrm{p}}/\tau_{\alpha,\mathrm{K}}$ in the deeply supercooled regime for different penetrant shapes in Fig.13. For 3D compact penetrants, because the degree of asymmetry of all shaped penetrants are very close and their nearly collapsed elastic barriers are relatively limited, one sees essentially negligible variation of $\tau_{\alpha,\mathrm{p}}/\tau_{\alpha,\mathrm{K}}$ with penetrant shape in Fig.13c.

We find all the above predictions in polymer melts qualitatively hold for crosslinked networks. Quantitatively, the decoupling time ratio is smaller for networks and decreases more sharply in the deeply supercooled regime within the same window of T_g/T or 1000K/T. These conclusions follow from our calculations of $\tau_{\alpha,p}/\tau_{\alpha,K}$ presented in Fig.S4.

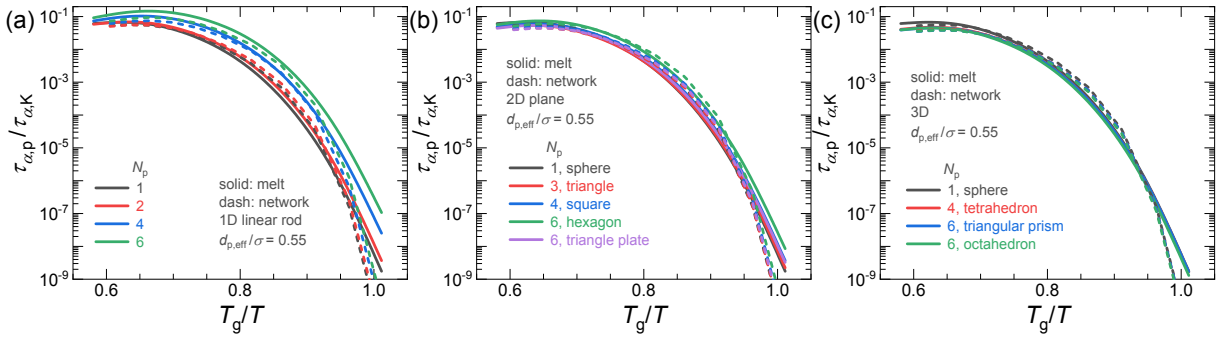

Fig.14. Same displays as in Fig.13 for the degree of decoupling between penetrant and Kuhn segment dynamics as quantified by the ratio of their alpha times, $\tau_{\alpha,p}/\tau_{\alpha,K}$, as a function of T_g/T in both the polymer melt (solid) and heavily crosslinked network (dash) for various 1D (a), 2D (b) and 3D (c) penetrant shapes, but now for the smaller penetrant size of $d_{eff}/\sigma = 0.55$.

For smaller penetrant systems ($d_{eff}/\sigma = 0.55$) with negligible elastic barriers we find the time ratio $\tau_{\alpha,p}/\tau_{\alpha,K}$ has a very limited penetrant shape dependence (see Fig.14), consistent with Figs.9a-9c. Additionally, the decoupling time ratio results of the same penetrant shape in melts versus networks are nearly collapsed, in agreement with prior findings for spherical penetrants [28]. This collapsed behavior continues to hold for spherical models for the larger size penetrants studied here ($d_{eff}/\sigma = 0.8$), as shown in Fig.13a. However, it fails for the larger non-spherical penetrants of high enough aspect ratios since their elastic barriers become very important. We expect that for large enough spherical penetrants where the elastic barrier is crucial, this collapsed behavior will not work as well, which we have confirmed (not shown for $d_{eff}/\sigma > 1.1$ cases).

We hope future experiments can test the above predictions in the deeply supercooled regime, especially the predicted strong decrease of the decoupling alpha timescale ratio.

B. Mechanistic aspects of decoupling: Evolution of $r_K - r_{K,c}$ and γ

By dissecting the origin of the theoretical predictions for the activated relaxation times, we have determined the mechanistic origin of decoupling in SCCH theory as a consequence of the behavior of the penetrant jump distance Δr_{p}, the facilitation displacement of Kuhn segments at the penetrant alpha time scale $\Delta r_{\mathrm{K,c}}$, the displacement difference of a Kuhn segment at its alpha time scale relative to that at the penetrant alpha time scale, $r_{\mathrm{K}} - r_{\mathrm{K,c}}$, and the trajectory coupling parameter, γ (see the definition of, and schematic for, these variables in Fig.4). These fundamental quantities underlie the physics of our alpha time ratio decoupling predictions and thus provide major insight, though they are difficult or impossible to directly measure. Given the latter fact, here we provide a compact summary of our analysis with all details documented in the SI. Readers not interested in these theoretical details can skip this subsection. For simplicity, we study these properties mainly by considering the 1D rod models.

As discussed above, the cross packing correlation quantity $N_{\mathrm{p}} g_{\mathrm{mp}}(d_{\mathrm{mp}})$ increases as N_{p} grows, implying a more compact polymer packing around the penetrant leads to a decrease of the penetrant jump distance with N_{p}, as documented in Fig.S5a for melts. In contrast to the behavior of Δr_{p}, the Kuhn segment cooperative facilitation displacement at the penetrant alpha time, $\Delta r_{\mathrm{K,c}}$, increases with N_{p} (see Fig.S5b). The reason is that for a larger N_{p} or penetrant aspect ratio, the multi-site penetrant can interact with more neighboring polymer monomers and hence is more coupled with their motion, which translates to a smaller value of the trajectory coupling constant γ (a value of unity is a kind of "slaving limit" [25, 26]). It is the combined effects of penetrant shape on Δr_{p} and γ that then leads to the increase of $\Delta r_{\mathrm{K,c}} = \Delta r_{\mathrm{p}}/\gamma$ with N_{p}. Moreover, as a multi-site penetrant interacts more with the surrounding polymer matrix, the influence of polymer matrix collective elasticity on penetrant hopping grows.

As discussed previously [28], the displacement difference variable $\Delta r_{\mathrm{K}} - \Delta r_{\mathrm{K,c}}$ reflects the magnitude of trajectory coupling between the penetrant and polymer. This quantity increases with inverse temperature (see Fig.15a), implying the degree of activated trajectory coupling decreases with cooling. This trend becomes less obvious as the penetrant aspect ratio grows.

Penetrants in crosslinked networks are predicted to move a larger distance before escaping their cage relative to in the analogous melt, and thus Δr_{p} in networks is higher than in melts (see Fig.S5a). Given γ does not change much with degree of crosslinking at fixed temperature or T_{g}/T (see Fig.15b and Figs.S7-S9), the Kuhn segment facilitation displacement $\Delta r_{\mathrm{K,c}} = \Delta r_{\mathrm{p}}/\gamma$ in networks is higher than in melts (Fig.S5b). Relative to the displacement at the penetrant alpha time scale $r_{\mathrm{K,c}}$, the Kuhn segment displacement at its alpha time scale, r_{K}, is more significantly affected by crosslinking (see Figs.S5b and S6b), resulting in a larger $r_{\mathrm{K}} - r_{\mathrm{K,c}}$ for networks than in melts (see Fig.15a). This indicates the degree of trajectory coupling in networks is less than in melts for common values of T_{g}/T, consistent with our findings based on the decoupling time ratio $\tau_{\alpha,\mathrm{p}}/\tau_{\alpha,\mathrm{K}}$.

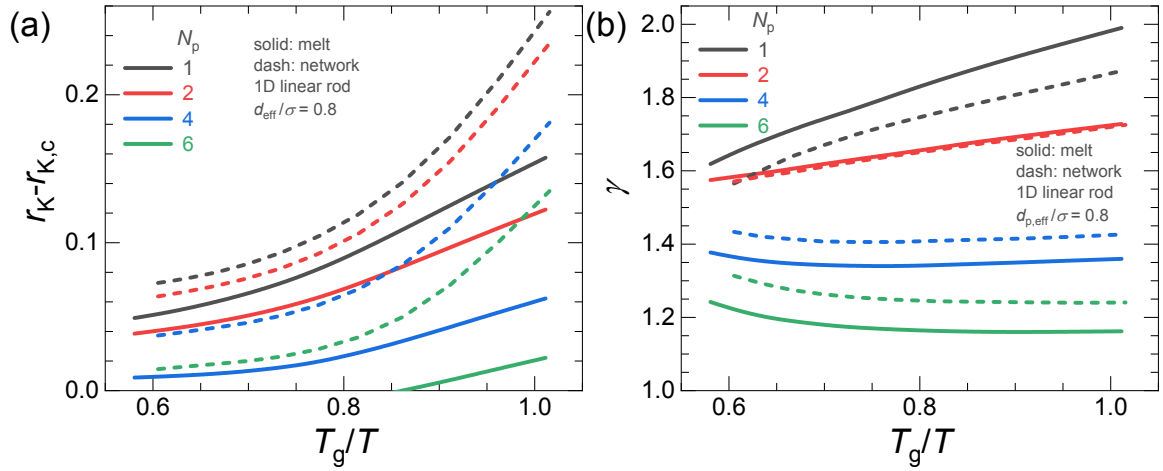

Fig.15. (a) The Kuhn segment displacement difference at its alpha time scale relative to that at the penetrant alpha time scale, $r_{\mathrm{K}} - r_{\mathrm{K,c}}$, and (b) the self-consistently determined trajectory coupling parameter, γ, as a function of T_{g}/T in the polymer melt (solid) and heavily crosslinked network (dash) for a wide range of 1D penetrant shapes and a penetrant size of $d_{\mathrm{eff}}/\sigma = 0.8$.

Example results for the trajectory coupling parameter γ are shown in Fig.15b. Because of the coupled penetrant-matrix nature of activated in SCCH theory, γ enters only via its effect on local cage barriers (see the SI and refs. [25-28]). Its evolution with temperature, crosslink density, penetrant shape, and temperature differ slightly from that of $r_{\mathrm{K}} - r_{\mathrm{K,c}}$ or the alpha time ratio $\tau_{\alpha,\mathrm{p}}/\tau_{\alpha,\mathrm{K}}$. We find these behaviors are very similar for both penetrant sizes studied here, as confirmed by comparing results in Figs.15b, S7, and S8. With decreasing temperature, γ varies only slightly, suggesting the decoupling of the *local cage* dynamics of penetrant and polymer monomers is weakly dependent on temperature. However, interestingly, whether γ increases, decreases, or remains constant with temperature does depend significantly on penetrant shape. Specifically, γ increases as temperature decreases in the penetrant low aspect ratio regime and the increase of slope of the γ versus T_{g}/T plot decreases with aspect ratio. On the other hand, as shown in Fig.15b, increasing penetrant aspect ratio to a large enough value results in a variation of γ with inverse temperature changing to a decaying behavior at high temperatures followed by a tendency to saturate at low temperatures. The physical reason is that as penetrant aspect ratio increases, the degree of trajectory coupling increases significantly, and eventually the penetrant dynamics is effectively dynamically slaved to its polymer neighbors leading to the quasi-plateau feature in Fig.15b in the deeply supercooled regime. These behaviors remain qualitatively the same when changing from polymer melts to networks, with only minor quantitative differences (see Fig.15b).

Finally, we note that our results for both $r_{\mathrm{K}} - r_{\mathrm{K,c}}$ and γ in Figs.15a and 15b imply that the degree of decoupling decreases significantly as the penetrant aspect ratio grows in melts and networks. However, a different temperature dependence is predicted due to the unimportance of collective elasticity in the self-consistent determination of γ, which provides further evidence that

the significant increase of decoupling with cooling of the alpha time ratios in the deeply supercooled regime is mainly originated from the effect of elasticity.

VI. Experimental Implications and Applications

A. Experimental and materials science significance

With the goal of stimulating new experimental and simulation tests of our theory, and potential exploitation in materials science applications, we briefly summarize key testable predictions based on our analysis of shaped penetrants in polymer melts and networks.

(i) Figures 5 to 8 predict significant shape effects *at fixed molecular volume* on the penetrant relaxation time over a wide range of temperatures and two crosslink densities (zero per melts, and very high per tight networks) in both absolute temperature and reduced inverse temperature T_g/T spaces. The penetrant alpha time (and inverse diffusivity) significantly increases with aspect ratio, particularly in the deeply supercooled regime. The shape effects in melts on penetrant dynamics is much weaker over the same temperature range in absolute temperature space, while the trend is opposite in T_g/T space over the same T_g/T range. The former trend is of high practical relevance given applications such as membrane separations are generally pursued at a fixed temperature. Under this condition, a crosslinked network membrane can deliver a relatively larger selectivity between different shaped molecules of the same volume compared to a melt matrix. We note also that different solvation conditions can induce short flexible chain molecules (such as alkanes) to take on different conformations and statistical shapes. Hence, our results may be germane to how changes of penetrant shape at constant molecular volume affect the penetrant transport rate of such important molecules.

(ii) Relative to larger sized penetrants, the shape effect on smaller size penetrants is much more limited, and their behavior is very similar in melts and networks. The reason is that for larger penetrants, both the elastic and local cage barriers are crucial and the shape effect on the penetrant elastic barrier is predicted to be much more pronounced, while for small penetrants only the relatively shape insensitive local cage barrier is important. Thus, the shape effect studied in both the weak and intermediate polymer supercooled regime is predicted to be not very important regardless of penetrant size, thereby suggesting membrane separation applications related to shape selectivity at fixed penetrant volume should be performed in the deeply supercooled regime. In a recent simulation work [19], Kanduč et al. found evidence for an exponential law for the penetrant diffusion constant, $D_{\mathrm{p}} \propto \exp\left(-a_w/\lambda\right)$, at the relatively high temperatures accessible in simulation and for small/medium sized penetrants of effective molecular diameter a_w (Stokes radius or radius of gyration) studied, where here λ is a shape-dependent parameter using notation from ref.[19] (which is different and should be distinguished from λ used above as the penetrant aspect ratio). This finding is in qualitative agreement with early SCCH theory studies [26] based on a spherical penetrant in a sphere matrix model. According to our more recent findings based on SCCH theory for dilute penetrants in explicitly polymer matrices[27, 29, 31], complementary computer simulations[31], and experiments on larger aromatic penetrants[29, 31], the penetrant diffusion constant follows such an exponential behavior when the penetrant has a relatively small or medium size and the system is not too deeply supercooled, in agreement with Kanduč et al.[19]] However, for larger penetrants in cold matrices, a more power law like correlation appears [29, 31]. Taken together, these findings suggest that under the moderate supercooled conditions simulated and for not too large penetrants, elastic barriers play a minor role. We believe this is the reason for the predicted unimportance of shape effects at fixed molecular volume, and for our present finding

that shape effects *at fixed* molecular volume enter mainly via the collective elastic barriers. This deduction seems to be in accord with the finding by Kanduč et al. that their parameter λ varies weakly in their simulation data analysis[19].

(iii) A dimensionless length scale ratio, the "penetrant aspect ratio" variable $\lambda/\sigma = (2R_{\mathrm{g}} + d_{\mathrm{s}})/\sigma$, theoretically organizes quite well the numerically discovered trends related to the nature and magnitude of penetrant shape effects. We hope future experimental and simulation work can test this.

(iv) The alpha time decoupling ratio $\tau_{\alpha,\mathrm{p}}/\tau_{\alpha,\mathrm{K}}$ can be measured. We predict it varies in a weakly non-monotonic manner with temperature, and is significantly size ratio and penetrant shape dependent. The microscopic displacement difference quantity, $r_{\mathrm{K}} - r_{\mathrm{K,c}}$, is also important theoretically, but our predictions for it can likely only be tested in carefully designed simulations.

B. Application to penetrant diffusion experiments

Here we consider a testable prediction for how penetrant shape influences the magnitude and temperature dependence of the diffusion constant of specific penetrants in the crosslinked PnBA network studied experimentally previously [29]. Per our prior theoretical work on spherical penetrant dynamics in crosslinked networks [28, 30], and as discussed in section III-B above, we established that geometric entropic mesh confinement in crosslinked networks is a minor effect, and to leading order the penetrant diffusion constant is proportional to the inverse penetrant alpha time. Specifically, as found above in Fig.11, shape effects will not change the exponential relation between the penetrant alpha time and $\mathrm{T_g}(f_{\mathrm{n}})/T$, although the corresponding slope does change in the deeply supercooled regime for larger size penetrants. Thus, we argue that the analysis of temperature dependence of inverse penetrant alpha time should be applicable both quantitatively and qualitatively to the penetrant diffusion constant. Indeed, prior experiments found in variable

crosslinked networks [29] an exponential relationship between the penetrant diffusion constant and $T_g(f_n)/T$ at fixed temperature, with systematic variation as a function of penetrant size and shape, consistent with the predictions of SCCH theory.

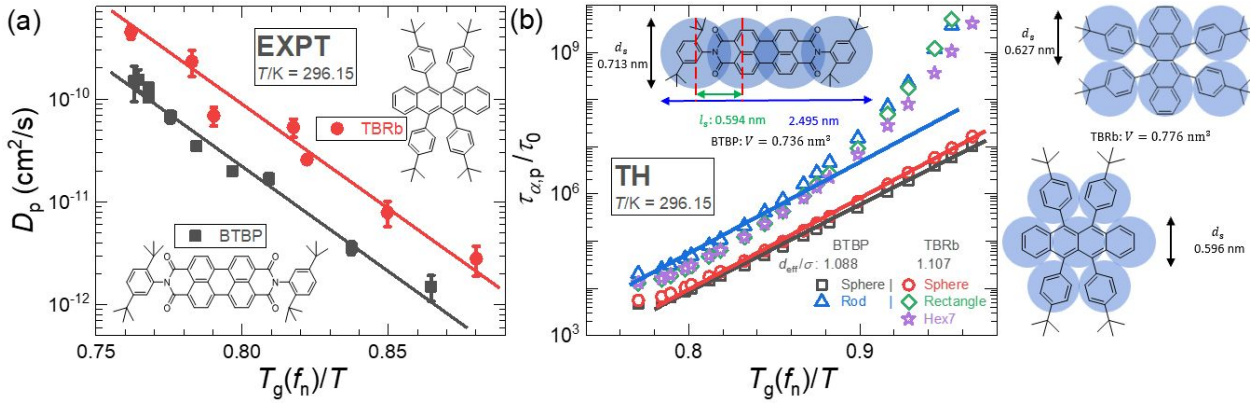

Fig.16. (a) Log − linear plot of the experimental (EXPT) diffusion constants of dilute BTBP or TBRb in PnBA networks as a function of $T_g(f_n)/T$ over a wide range of crosslink fractions at T = 296.15 K (23℃). (b) Theoretically predicted mean alpha time of dilute BTBP or TBRb in the PnBA networks as a function of $T_g(f_n)/T$ at T = 296.15K. For BTBP, we have considered two shape models: (i) an effective sphere model of diameter [29] $d_{\text{eff}} = (6V_{\text{BTBP}}/\pi)^{1/3} = 1.12$ nm with $V_{\text{BTBP}} = 0.736$ nm^3 the known experimental effective molecular volume of BTBP [58] and (ii) a four-site overlapped rod model as shown in the inset of (b) where the diameter of each site is $d_s = 0.713$ nm and the distance between two neighbor sites is $l_s = 0.594$ nm, which are calculated based on the facts that $V_{\text{BTBP}} = 0.736$ nm^3 and the length ratio of long-axis to short-axis is ~3.5 [58]. For TBRb, we also consider the spherical model with $d_{\text{eff}} = (6V_{\text{TBRb}}/\pi)^{1/3} = 1.14$ nm and $V_{\text{TBRb}} = 0.776$ nm^3. Two non-spherical shape models are considered for TBRb as shown in the far-right panel of (b): (i) the six-site rectangle model with $d_s = d_{\text{eff}}/\sqrt{6} = 0.627$ nm and (ii) the seven-site hexagon-like (Hex7) model with $d_s = d_{\text{eff}}/\sqrt{7} = 0.596$ nm.

Fig.16a re-plots the experimental diffusion constant [29] as a function of $T_g(f_n)/T$ for BTBP and TBRb in PnBA networks. Recall that these two penetrants have significantly different shapes but essentially identical molecular volumes. It is experimentally observed that both diffusion constants decrease exponentially with $T_g(f_n)/T$ with a nearly *identical slope* over the range of $0.76 < T_g(f_n)/T < 0.88$. Such behavior is consistent with our theory predictions in Fig.11 over the range $0.76 < T_g(f_n)/T < 0.88$ for both penetrant sizes ($d_{\text{eff}}/\sigma = 0.55$ and 0.8).

To pursue a quantitative analysis, we evaluate the effective diameter of BTBP and TBRb based on their reported volumes [29] (see caption of Fig.12). We find the ratio d_{eff}/σ of BTBP and TBRb (diameters of 1.12 nm and 1.14nm, respectively) to the PnBA bare bead size (given in section IIIA, $\sigma = 1.03$ nm) is 1.088 and 1.107, respectively, virtually identical. Employing these numbers in the *spherical penetrant* model in SCCH theory delivers nearly the same values of alpha time and diffusion constant for BTBP and TBRb. However, as shown in Fig.16a, the diffusion constant of TBRb is experimentally larger than that of BTBP by a modest factor of ~5, in contrast to treating these penetrants as spheres (see red and black data in Fig.16b). Hence, these measurements clearly show a non-negligible shape effect at fixed penetrant volume [29].

BTBP [58] is roughly rod-like with an aspect ratio (long-to-short length scales) of ~3.5. This motivates us to model it as a four overlapping site rod where the site bead diameter d_{s} is not the same as the site-site bond length l_{s}. As shown in the inset of Fig.16b, for this model one can then calculate $d_{\text{s}} = 0.713$ nm (also identified as the short-axis length), the long-axis length as 2.495 nm, and the bond length as 0.594 nm based on an aspect ratio of 3.5 and $V_{\text{BTBP}} = 0.736$ nm^3. In contrast, TBRb has a planar-like shape and higher symmetry compared to BTBP. We have thus constructed two special model shapes for TBRb: a 6-site rectangle model and a 7-site hexagon-like (Hex7) model (see schematic in the far-right panel of Fig.16b). For simplicity, for the rectangle and Hex7 models we use tangent sites with $d_{\text{s}} = 0.627$ nm and 0.596 nm, respectively.

Figure 16b presents the theoretical predictions of the alpha time for the three model penetrants (4-site overlapped BTBP, 6-site rectangle TBRb, and Hex7 TBRb) and also for the two spherical penetrant models of the same space filling volume; the temperature is fixed to the experimental value of 296.15K. One observes that for the two spherical models, $\tau_{\alpha,\text{p}}/\tau_0$ of TBRb is only slightly higher than that of BTBP because the molecular volume of TBRb is very close to,

but slightly larger than, the BTBP volume. When changing from the effective hard sphere description of BTBP to the 4-site overlapped rod model, an approximately 1 decade increase in $\tau_{\alpha,\mathrm{p}}/\tau_0$ is predicted, while within the experimental temperature range of $0.76 < T_{\mathrm{g}}(f_{\mathrm{n}})/T < 0.88$ a linear relationship between $\log(\tau_{\alpha,\mathrm{p}}/\tau_0)$ and $T_{\mathrm{g}}(f_{\mathrm{n}})/T$ still applies. However, in the *deeply* supercooled regime this linear relationship, which is theoretically predicted and confirmed in the *weakly* supercooled regime, is theoretically predicted to fail when the significantly bent-upward behavior appears as seen in Fig.16b corresponding to a "non-Arrhenius" like growth. The reason for this upturn is that the effective diameter ratio of BTBP (and TBRb) to polymer site diameter (1.03 nm) is large enough that the elastic barrier is highly important in the deeply supercooled regime which enhances the slowing down of penetrant hopping.

For TBRb, when changing from a hard sphere model description to the rectangle or Hex7 model, the predicted $\tau_{\alpha,\mathrm{p}}/\tau_0$ is increased by a factor of ~5-6. This modestly smaller factor than predicted for BTBP seems intuitive based on the theory given TBRb is a more compact planar or 2D-like molecule versus the rod-like or more 1D-like nature of BTBP. In terms of our more refined models, the absolute value of $\tau_{\alpha,\mathrm{p}}/\tau_0$ thus becomes smaller than that for the 4-site overlapped rod model of BTBP by a factor of ~2 in the window of $0.76 < T_{\mathrm{g}}(f_{\mathrm{n}})/T < 0.88$ where the linear Arrhenius-like relationship remains valid and has the same slope as that of BTBP 4-sites rod model, as shown in Fig.16b.

The above theoretical predictions are consistent with the experimental results in Fig.16a with regards to (a) the linearity of the log-linear plot, (b) the same slope, and (c) the alpha time (diffusion constant) of BTBP is higher (lower) than that of TBRb. However, the precise absolute value of the difference in diffusion constants is experimentally a factor of ~5-6 between TBRb and BTBP, while the difference in theoretical alpha times is a smaller factor of ~2. This difference may

be (at least partially) a consequence of the vagaries of how to model the non-spherical shapes of the two molecules within the class of coarse-grained models we have adopted. But overall, we find our results to be encouraging and consistent with experiment, and provide further support for the proposed zeroth order idea of significant self-averaging (at fixed molecular volume) importance of shape at fixed molecular volume for activated penetrant transport, but with non-negligible quantitative differences due to shape.

Finally, we emphasize that in the deeply supercooled regime not yet probed experimentally, both the rectangle and Hex7 models for TBRb display an upwardly curved growth of their hopping or relaxation time, with $\log(\tau_{\alpha,\mathrm{p}}/\tau_0)$ vs $T_{\mathrm{g}}(f_{\mathrm{n}})/T$ roughly of a parabolic form. This is an experimentally testable prediction, and is consistent with that of the 4-site rod model of BTBP due to the dominant role of penetrant elastic barriers in the deeply supercooled regime.

Considering the similarity within our theory of the temperature dependence of the penetrant diffusion constant and the inverse penetrant alpha time, one can combine the results in Fig.11 and Fig.16 to deduce qualitative scaling law forms as a function of $T_{\mathrm{g}}(f_{\mathrm{n}})/T$. From Fig.11 for a small and medium size penetrant, we find to leading order an exponential relationship between inverse diffusion constant or relaxation time and $T_{\mathrm{g}}(f_{\mathrm{n}})/T$, per $\log(1/D_{\mathrm{p}}) or \log(\tau_{\alpha,\mathrm{p}}) = a + bT_{\mathrm{g}}(f_{\mathrm{n}})/T$, with the prefactor "$b$" increasing with cooling and being shape-dependent. The shape-dependent trends are particularly important in the deeply supercooled regime for the larger size penetrant where the slope b changes dramatically with molecular shape. This is a predicted consequence of the importance of the collective elastic barrier for relatively large penetrants under cold conditions. For the D_{p} calculations in Fig.16, we note that the experimental penetrants are larger than both sizes studied in Fig.11. Here we find a scaling law between D_{p} and $T_{\mathrm{g}}(f_{\mathrm{n}})/T$ again of an exponential form in the smaller $T_{\mathrm{g}}(f_{\mathrm{n}})/T$ (i.e., more weakly supercooled) regime where the local

cage barrier is dominant, $\log(1/D_{\mathrm{p}}) or \log(\tau_{\alpha,\mathrm{p}}) = a + bT_{\mathrm{g}}(f_{\mathrm{n}})/T$. In contrast, in the more deeply supercooled regime [larger $T_{\mathrm{g}}(f_{\mathrm{n}})/T$], we predict a roughly parabolic form $\log(1/D_{\mathrm{p}})$ or $\log(\tau_{\alpha,\mathrm{p}}) = a + bT_{\mathrm{g}}(f_{\mathrm{n}})/T + c[T_{\mathrm{g}}(f_{\mathrm{n}})/T]^2$, where the parameters a, b, and c are shape-dependent (see Fig.16b, the difference in magnitude between purple star and green diamond symbols but with nearly the same slope).

VII. Summary and Discussion

We have carried out a detailed statistical mechanical theory study (the first of its kind to the best of our knowledge) of how molecular shape influences the activated hopping driven relaxation and diffusion of dilute penetrants in polymer melts and crosslinked networks over a very wide range of temperatures and penetrant shapes. The key new methodological aspect is a general extension of the SCCH theory of penetrant activated hopping previously formulated for spherical penetrants to address the dynamic consequences of non-spherical penetrant shape on translational motion. As penetrant shape becomes less globular or compact (increasing aspect ratio or degree of asymmetry), its solvation packing by the dense polymer matrix changes and the penetrant can contact more surrounding monomers, which results in a rich behavior of penetrant relaxation time as a function of temperature, crosslink density, and penetrant shape.

The penetrant local cage barrier is predicted to vary in only a very limited manner with penetrant shape, while its collective elastic barrier increases significantly with penetrant shape asymmetry in the deeply supercooled regime. We believe this is a key insight in the search for how to successfully separate molecules of the same space filling volume but different shapes. For a relatively small size penetrant or at high enough temperatures, the penetrant local cage barrier is far larger than its corresponding essentially negligible elastic barrier, and penetrant shape effects

are very weak. On the other hand, for a larger size penetrant at low temperatures, the penetrant hopping process has a strong shape dependence due to the importance of collective elasticity.

We have compared the penetrant shape effects on temperature-dependent activated penetrant relaxation in polymer melts and crosslinked networks, and find opposite trends in the T_g/T and $1000\mathrm{K}/T$ representations. In T_g/T space, the shape effect on the penetrant alpha time is stronger and its absolute value is higher in melts than that in the heavily crosslinked network over the same range of T_g/T. However, in $1000\mathrm{K}/T$ space, the shape effect on the penetrant alpha time is weaker and its absolute value is smaller in melts than that in networks over the same temperature range, mainly due to slower polymer monomer relaxation under crosslinked network conditions.

Different microscopic variables were explored to describe the relaxation time decoupling and trajectory-level coupling between the activated dynamics of penetrants and polymer Kuhn segments. We find that penetrant shape does play a significant role in the deeply supercooled regime for these quantities for relatively large penetrants because of the importance of penetrant-shape dependent elastic effects. The elastic barrier is also relevant to how penetrant shape affects the crosslinking dependence of the penetrant alpha time or diffusion constant. For example, in the weak or intermediate supercooled regime, the exponential relationship (including the slope) between penetrant diffusion constant and crosslink density remains unchanged with varying penetrant shape. However, in the deeply supercooled regime where collective elasticity becomes crucial, the exponential relationship between penetrant diffusion constant and crosslink density is significantly penetrant-shape dependent. Considering the importance of shape effects on penetrant dynamics, we also proposed a dimensionless "aspect ratio" variable $\lambda/\sigma = (2R_g + d_s)/\sigma$ to organize the penetrant dynamics behavior with shape, and showed that it works well.

Finally, there are several possible extensions of the present theoretical approach and modeling strategy. Given many non-spherical penetrants have a more open, non-globular structure compared to their spherical analog, introducing chemistry-specific penetrant-polymer attractive interactions (as done theoretically for spherical penetrants [27]) for non-spherical penetrants may provide a promising direction to improve selectivity. Another topic is the role of external stress [41], which decreases the elastic effects significantly while the local cage barrier is affected much less. Other possible directions include how to control the selectivity of non-spherical penetrants in dynamic bond forming vitrimers and associating polymer matrices [59-62], and whether dynamic heterogeneity [63-67] effects can modify penetrant shape effects on diffusion selectivity. Work is underway in these directions.

Conflicts of interest

There are no conflicts to declare.

Acknowledgement

This research was supported by the U.S. Department of Energy, Office of Basic Energy Sciences, Division of Materials Sciences and Engineering Award No. DE-SC0020858 through the Materials Research Laboratory at the University of Illinois at Urbana-Champaign. Helpful discussions with Professors Christopher Evans and Charles Sing are gratefully acknowledged.

References

1 L.-H. Cai, S. Panyukov and M. Rubinstein, *Macromolecules*, 2015, **48**, 847.
2 G. S. Sheridan and C. M. Evans, *Macromolecules*, 2021, **54**, 11198.
3 V. Sorichetti, V. Hugouvieux and W. Kob, *Macromolecules*, 2021, **54**, 8575.
4 Z. Xu, X. Dai, X. Bu, Y. Yang, X. Zhang, X. Man, X. Zhang, M. Doi and L.-T. Yan, *ACS nano*, 2021, **15**, 4608.

5 W. J. Koros and R. Mahajan, *J. Membr. Sci.*, 2000, **175**, 181.
6 D. F. Sanders, Z. P. Smith, R. Guo, L. M. Robeson, J. E. McGrath, D. R. Paul and B. D. Freeman, *Polymer*, 2013, **54**, 4729.
7 J. S. Vrentas and C. M. Vrentas, *Diffusion and mass transfer*, CRC Press, Boca Raton, 2016.
8 M. Galizia, W. S. Chi, Z. P. Smith, T. C. Merkel, R. W. Baker and B. D. Freeman, *Macromolecules*, 2017, **50**, 7809.
9 J. W. Barnett and S. K. Kumar, *Soft matter*, 2019, **15**, 424.
10 C. R. Bilchak, M. Jhalaria, Y. Huang, Z. Abbas, J. Midya, F. M. Benedetti, D. Parisi, W. Egger, M. Dickmann and M. Minelli, *ACS nano*, 2020, **14**, 17174.
11 B. J. Blaiszik, S. L. B. Kramer, S. C. Olugebefola, J. S. Moore, N. R. Sottos and S. R. White, *Ann. Rev. Mater. Res.*, 2010, **40**, 179.
12 J. F. Patrick, M. J. Robb, N. R. Sottos, J. S. Moore and S. R. White, *Nature*, 2016, **540**, 363.
13 G. M. Geise, D. R. Paul and B. D. Freeman, *Prog. Polym. Sci.*, 2014, **39**, 1.
14 L.-C. Dong and A. S. Hoffman, *J. Controlled Release*, 1990, **13**, 21.
15 N. A. Peppas, *Curr. Opin. Colloid Interface Sci.*, 1997, **2**, 531.
16 J. Li and D. J. Mooney, *Nat. Rev. Mater.*, 2016, **1**, 16071.
17 Y. Tamai, H. Tanaka and K. Nakanishi, *Macromolecules*, 1994, **27**, 4498.
18 J. G. Wijmans and R. W. Baker, *J. Membr. Sci.*, 1995, **107**, 1.
19 M. Kanduč, W. K. Kim, R. Roa and J. Dzubiella, *ACS nano*, 2020, **15**, 614.
20 J. S. Vrentas and J. L. Duda, *J. Polym. Sci. B-Polym. Phys.*, 1977, **15**, 403.
21 N. Ramesh, P. K. Davis, J. M. Zielinski, R. P. Danner and J. L. Duda, *J. Polym. Sci. B-Polym. Phys.*, 2011, **49**, 1629.
22 K. Zhang and S. K. Kumar, *ACS Macro Lett.*, 2017, **6**, 864.
23 D. Meng, K. Zhang and S. K. Kumar, *Soft matter*, 2018, **14**, 4226.
24 K. Zhang, D. Meng, F. Müller-Plathe and S. K. Kumar, *Soft matter*, 2018, **14**, 440.
25 B. Mei and K. S. Schweizer, *Soft Matter*, 2021, **17**, 2624.
26 R. Zhang and K. S. Schweizer, *J. Chem. Phys.*, 2017, **146**, 194906.
27 B. Mei and K. S. Schweizer, *Macromolecules*, 2022, **55**, 9134.
28 B. Mei, T.-W. Lin, C. E. Sing and K. S. Schweizer, *J. Chem. Phys.*, 2023, **158**, 184901.
29 B. Mei, T.-W. Lin, G. S. Sheridan, C. M. Evans, C. E. Sing and K. S. Schweizer, *ACS Cent. Sci.*, 2023, **9**, 508.
30 T.-W. Lin, B. Mei, K. S. Schweizer and C. E. Sing, *J. Chem. Phys.*, 2023, **159**, 014904.
31 B. Mei, G. S. Sheridan, C. M. Evans and K. S. Schweizer, *Proc. Natl. Acad. Sci. USA*, 2022, **119**, e2210094119.
32 B. Mei, Y. Zhou and K. S. Schweizer, *Proc. Natl. Acad. Sci. USA*, 2021, **118**, e2025341118.
33 S. Mirigian and K. S. Schweizer, *J. Chem. Phys.*, 2014, **140**, 194506.
34 B. Mei, Y. Zhou and K. S. Schweizer, *J. Phys. Chem. B*, 2020, **124**, 6121.

35 Y. Zhou, B. Mei and K. S. Schweizer, *J. Chem. Phys.*, 2022, **156**, 114901.
36 B. Mei, Y. Zhou and K. S. Schweizer, *Macromolecules*, 2021, **54**, 10086.
37 S. J. Xie and K. S. Schweizer, *Macromolecules*, 2016, **49**, 9655.
38 S. Mirigian and K. S. Schweizer, *Macromolecules*, 2015, **48**, 1901.
39 S. Mirigian and K. S. Schweizer, *J. Chem. Phys.*, 2014, **140**, 194507.
40 B. Mei, T.-W. Lin, G. S. Sheridan, C. M. Evans, C. E. Sing and K. S. Schweizer, *Macromolecules*, 2022, **55**, 4159−4173.
41 B. Mei and K. S. Schweizer, *J. Chem. Phys.*, 2021, **155**, 054505.
42 K. S. Schweizer and J. G. Curro, *Adv. Chem. Phys.*, 1997, **1**.
43 K. S. Schweizer and J. G. Curro, *Phys. Rev. Lett.*, 1987, **58**, 246.
44 K. G. Honnell, J. G. Curro and K. S. Schweizer, *Macromolecules*, 1990, **23**, 3496.
45 R. Koyama, *J. Phys. Soc. Jpn.*, 1973, **34**, 1029.
46 B. Mei, Y. Zhou and K. S. Schweizer, *J. Phys. Chem. B*, 2021, **125**, 12353.
47 M. Tripathy and K. S. Schweizer, *J. Chem. Phys.*, 2009, **130**, 244907.
48 M. Tripathy and K. S. Schweizer, *J. Chem. Phys.*, 2009, **130**, 244906.
49 G. Yatsenko and K. S. Schweizer, *Phys. Rev. E*, 2007, **76**, 041506.
50 G. Yatsenko and K. S. Schweizer, *J. Chem. Phys.*, 2007, **126**, 014505.
51 J.-P. Hansen and I. R. McDonald, *Theory of simple liquids*, Elsevier, Amsterdam, 2006.
52 D. Chandler, *Introduction to modern statistical mechanics*, Oxford University Press, Oxford, UK, 1987.
53 H. A. Kramers, *Physica*, 1940, **7**, 284.
54 P. Hänggi, P. Talkner and M. Borkovec, *Rev. Mod. Phys.*, 1990, **62**, 251.
55 R. Zhang and K. S. Schweizer, *J. Chem. Phys.*, 2010, **133**.
56 R. Zhang and K. S. Schweizer, *Phys. Rev. E*, 2009, **80**, 011502.
57 X.-J. Ma and R. Zhang, *Soft Matter*, 2023, **19**, 4746.
58 D. Ben-Amotz and J. M. Drake, *J. Chem. Phys.*, 1988, **89**, 1019.
59 L. Rovigatti, G. Nava, T. Bellini and F. Sciortino, *Macromolecules*, 2018, **51**, 1232.
60 A. Perego and F. Khabaz, *Macromolecules*, 2020, **53**, 8406.
61 A. Perego, D. Lazarenko, M. Cloitre and F. Khabaz, *Macromolecules*, 2022, **55**, 7605.
62 L. Porath, B. Soman, B. B. Jing and C. M. Evans, *ACS Macro Lett.*, 2022, **11**, 475.
63 L. Berthier and G. Biroli, *Rev. Mod. Phys.*, 2011, **83**, 587.
64 S.-J. Xie and K. S. Schweizer, *Macromolecules*, 2020, **53**, 5350.
65 S.-J. Xie and K. S. Schweizer, *J. Chem. Phys.*, 2020, **152**, 034502.
66 B. Mei, B. Zhuang, Y. Lu, L. An and Z.-G. Wang, *J. Phys. Chem. Lett.*, 2022, **13**, 3957.
67 B. Mei, Y. Lu, L. An and Z.-G. Wang, *Phys. Rev. E*, 2019, **100**, 052607.